Speromagnetism and asperomagnetism as the ground states of the Tb-Dy-Ho-Er-Tm "ideal" high-entropy alloy

M. Krnel [a], S. Vrtnik [a], A. Jelen [a], P. Koželj [a,b], Z. Jagličić [c,d], A. Meden [e], M. Feuerbacher [f,§], J. Dolinšek [a,b,*]

[a] *Jožef Stefan Institute, Solid State Physics Department, Jamova 39, SI-1000 Ljubljana, Slovenia*

[b] *University of Ljubljana, Faculty of Mathematics and Physics, Jadranska 19, SI-1000 Ljubljana, Slovenia*

[c] *Institute of Mathematics, Physics and Mechanics, Jadranska 19, SI-1000 Ljubljana, Slovenia*

[d] *University of Ljubljana, Faculty of Civil and Geodetic Engineering, Jamova 2, SI-1000 Ljubljana, Slovenia*

[e] *University of Ljubljana, Faculty of Chemistry and Chemical Technology, Večna pot 113, SI-1000 Ljubljana, Slovenia*

[f] *Institut für Mikrostrukturforschung, Forschungszentrum Jülich, D-52425 Jülich, Germany*

* Corresponding author. Jožef Stefan Institute, Solid State Physics Department, Jamova 39, SI-1000 Ljubljana, Slovenia.

E-mail address: jani.dolinsek@ijs.si (J. Dolinšek).

§ Corresponding author. Institut für Mikrostrukturforschung, Forschungszentrum Jülich, D-52425 Jülich, Germany.

E-mail address: m.feuerbacher@fz-juelich.de (M. Feuerbacher)

Abstract

We address the nature of the collective magnetic state in an ideal high-entropy alloy (HEA), representing a magnetically concentrated system with all lattice sites occupied by localized magnetic moments and containing randomness and frustration due to chemical disorder. Being a "metallic glass on a topologically ordered lattice", HEAs possess simultaneously the properties of an ordered crystal and an amorphous glass. The influence of this crystal-glass duality on the collective magnetic state was studied experimentally on a hexagonal Tb-Dy-Ho-Er-Tm (TDHET) HEA, composed of rare-earth (RE) elements with zero pair mixing enthalpies that assure completely random mixing of the elements and very similar atomic radii that minimize lattice distortions, representing a prototype of an ideal HEA. The TDHET HEA is characterized by probability distributions of the atomic moments $P(\mu)$, the exchange interactions $P(\mathcal{J})$, the magnetocrystalline anisotropy $P(D)$, and the dipolar interactions $P(H_d)$. Based on the measurements of the static and dynamic magnetization, the magnetization $M(H)$ curves, the thermoremanent magnetization, the specific heat and the magnetoresistance, we found that the collective magnetic state of the TDHET is temperature-dependent, forming a speromagnetic (SPM) state in the temperature range between about 140 and 30 K and an asperomagnetic (ASPM) state below 20 K. In the intermediate temperature range between 30 and 20 K, a spin glass (SG) state is formed, representing a transition state between the speromagnetic and asperomagnetic states. The observed temperature evolution of the magnetic ground state in the TDHET HEA upon cooling in the sequence SPM→SG→ASPM is a result of temperature-dependent, competing magnetic interactions. The distribution of the exchange interactions $P(\mathcal{J})$ shifts continuously on the $\mathcal{J}$ axis from the high-temperature SPM-type with the average interaction biased towards a net

negative value, $\bar{\mathcal{J}} < 0$, through the SG-type with $\bar{\mathcal{J}} = 0$, to the low-temperature ASPM-type with $\bar{\mathcal{J}} > 0$. This shift is a band-structure effect, closely linked with the crystallinity of the spin system, which the TDHET HEA shares with the topologically ordered crystals. The probability distributions $P(\mu)$, $P(\mathcal{J})$, $P(D)$ and $P(H_d)$ are, on the other hand, a consequence of chemical disorder, a property that the TDHET HEA shares with the amorphous magnets. Both features, the topologically ordered lattice and the amorphous-type chemical disorder essentially determine the magnetic state of an ideal, RE-based HEA.

Keywords: A. high-entropy alloys; B. magnetic properties.

1. Introduction

An ideal high-entropy alloy (HEA) is by definition a solid solution of five or more chemical elements, distributed randomly on an undistorted crystal lattice. Such topologically ordered, but chemically (substitutionally) disordered system can be conveniently termed as a "*metallic glass on an ordered lattice*", possessing simultaneously the properties of an ordered crystal and an amorphous glass. A good approximation of an ideal HEA is a mixture of rare earth (RE) elements with zero pair mixing enthalpies between any pair of the elements i and j, $\Delta H_{mix}^{ij} = 0$, that leads to completely random mixing of the elements [1-4]. Extended solid solubility of the elements is augmented by choosing elements with the same crystal structure [5], whereas minimal lattice distortions are achieved by taking elements with very similar atomic radii r_i, so that the atomic-size-difference (geometric) parameter $\delta = \sqrt{\sum_{i=1}^{N} c_i(1 - r_i/\bar{r})^2}$ is minimized. Here N is the number of components, c_i is the molar concentration of the element i and $\bar{r} = \sum_i c_i r_i$ is the composition-averaged radius. A prototype of an ideal HEA is an equiatomic solid solution Tb-Dy-Ho-Er-Tm, composed of the elements from the heavy half of the lanthanide series. Pure metals all possess a hexagonal close-packed (hcp) structure at room temperature (RT), their pair mixing enthalpies are zero [6], and, being neighbors in the periodic system, the geometric parameter δ assumes the smallest value ($\delta < 0.5$ %) of all HEAs reported so far in the literature, so that the lattice distortions are minute. In our study, we have synthesized a $Tb_{20.3}Dy_{20.7}Ho_{20.3}Er_{19.7}Tm_{19.0}$ polycrystalline material of hexagonal symmetry (hcp structure, space group $P6_3/mmc$, lattice parameters a = 3.582(2) Å and c = 5.632(3) Å). Details of the material synthesis, the XRD (Fig. A1) and the SEM (Fig. A2) characterization are given in the Appendix A, whereas the properties

of pure elements and metals are collected in Table A1 of the Appendix A. The composition-averaged theoretical lattice parameters of this alloy $\bar{a}$ = 3.575 Å and $\bar{c}$ = 5.622 Å match almost perfectly the experimental ones, supporting random mixing of the elements, whereas minute value of the geometric parameter $\delta = 0.48$ % for this composition indicates an almost undistorted hcp lattice. The Tb-Dy-Ho-Er-Tm HEA (abbreviated in the following as TDHET) is thus an excellent physical realization of a metallic glass on a topologically ordered lattice.

Triply ionized elements Tb, Dy, Ho, Er and Tm all possess large, localized 4*f* magnetic moments of paramagnetic values $\mu^{Tb} = 9.72$, $\mu^{Dy} = 10.65$, $\mu^{Ho} = 10.61$, $\mu^{Er} = 9.58$, and $\mu^{Tm} = 7.56$ (in units of Bohr magnetons μ_B), so that TDHET is characterized by a random distribution of large atomic moments of different sizes on a hcp lattice, with all sites being magnetic. In a metallic environment, the localized 4*f* moments couple indirectly via the electrons in the 5*d*/6*s* conduction band, leading to the long-range oscillatory RKKY coupling between the moments. The effective coupling between two localized moments separated by r is $\mathcal{J}_{eff} \approx 9\pi\mathcal{J}_{sf}^2\nu^2F(\xi)/(64\varepsilon_F)$, where $\mathcal{J}_{sf}$ is the *sf* exchange integral, ν is the number of conduction electrons per atom, $F(\xi) = (sin\xi - \xi cos\xi)/\xi^4$ is the RKKY function with $\xi = 2k_Fr$ (where k_F is the Fermi wavevector) and ε_F is the Fermi energy. Since k_F is typically of the order 0.1 nm^{-1}, the sign of $\mathcal{J}_{eff}$ fluctuates on a scale of nm, with many shells of interacting neighbors having either positive or negative coupling. The RKKY coupling constant of two RE ions of angular momentum $\hbar\vec{J}$ and Landé factor g is $\mathcal{J}_{RKKY} = G\mathcal{J}_{eff}$, where $G = (g-1)^2J(J+1)$ is the de Gennes factor. For unlike ions $(\hbar\vec{J}_i, g_i)$ and $(\hbar\vec{J}_j, g_j)$, the de Gennes factor is modified to $G_{ij} = (g_i - 1)(g_j - 1)\sqrt{J_i(J_i+1)J_j(J_j+1)}$ [7]. It is known that the magnetic ordering temperatures of any series of RE metals or compounds with the same electronic band structure and similar lattice spacing scale with G (or G_{ij}), reflecting

scaling of the $\mathcal{J}_{RKKY}$ coupling constant by the same factor. In the TDHET lattice, all five types of magnetic ions experience the same band structure and lattice spacing, so it is straightforward to assume that the RKKY coupling between the ions i and j can be written as $\mathcal{J}_{RKKY}^{ij} = G_{ij}\mathcal{J}_{eff}$. Taking the g_i, J_i values of the five ions Tb, Dy, Ho, Er and Tm collected in Table A1, we show in Fig. 1a the de Gennes factor G_{ij} normalized to G_{TbTb} for all fifteen possible atomic pairs. An almost continuous distribution is observed from G_{TbTb} (the largest) to G_{TmTm} (the smallest, amounting to 11 % of G_{TbTb}). The first coordination shell of a given atom in the hcp structure of $P6_3/mmc$ symmetry is shown in the inset of Fig. 1a. Each atom lies in a hexagonal plane normal to the z-axis and has 12–fold coordination, with six neighbors in the same plane, and three neighbors each in the upper and lower planes. The central atom is RKKY-coupled to all neighbors, and there is an enormous number of possibilities on how to distribute five different elements randomly on the twelve sites of the first coordination shell. This indicates that in the TDHET crystal, there exists an enormous number of different local chemical environments and the exchange interaction is distributed with a broad distribution function $P(\mathcal{J})$ (dropping the subscript RKKY), which can be considered symmetric (e.g. Gaussian-like) around the mean value $\bar{\mathcal{J}}$, with a variance $\Delta\mathcal{J}$.

The triply ionized ions Tb, Dy, Ho, Er and Tm also possess markedly different single-ion magnetocrystalline anisotropy, originating from the electrostatic interaction of the 4*f* charge cloud with the crystal electric fields (CF). The CF interaction stabilizes a particular electronic orbital, whereas the spin-orbit interaction then leads to magnetic moment alignment in a specific crystallographic direction. The five types of ions differ in the shape of the 4*f* electron cloud, which is oblate (flattened) for Tb, Dy and Ho, and prolate (elongated) for Er and Tm. At RT, the dominant term in the single-ion anisotropy energy is the interaction of the 4*f* electric quadrupole moment Q_2

with the electric field gradient created by the charge distribution of the crystal at the RE site. Since $Q_2 < 0$ for oblate ions, the moments of Tb, Dy and Ho align in the hexagonal plane, whereas the moments of the prolate ions Er and Tm ($Q_2 > 0$) align along the perpendicular hexagonal direction. At low temperatures, the hexadecapole Q_4 and the 64-pole moment Q_6 of the 4*f* charge density expanded in spherical harmonics also become important in the anisotropy energy, which pull the Tb, Dy, and Ho moments out of the hexagonal plane and the Er and Tm moments away from the hexagonal axis in a temperature-dependent manner. In the TDHET crystal, there exist local easy directions $\vec{e}_i$ (energetically favorable directions) of the moments on the scale of an atom or a nanoscale volume, which wander randomly over a few nearest-neighbor distances, so that TDHET can be considered as a random local anisotropy system with a continuous distribution of local anisotropies $P(D)$, where the leading term in the anisotropy energy of the site *i* is $-D_i\left(\vec{e}_i \cdot \vec{J}_i\right)^2$. In 4*f* alloys, the single-ion anisotropy energy is usually sufficient to pin the local magnetization direction.

The magnetic dipolar interaction between the 4*f* localized moments in the chemically disordered TDHET lattice also varies from site to site, characterized by a distribution of the dipolar magnetic fields $P(H_d)$ in both magnitude and direction.

The TDHET HEA thus represents a magnetically concentrated system with all sites magnetic, containing randomness (five different types of spins are placed randomly on the hcp lattice) and frustration (no spin configuration can satisfy all the bonds and minimize the energy at the same time). Unlike the site-ordered crystalline magnetic systems, which are typically characterized by a few discrete values of the atomic moments μ, the exchange interaction $\mathcal{J}$, the anisotropy D and the dipolar interactions H_d, the TDHET HEA is characterized by probability distributions $P(\mu)$, $P(\mathcal{J})$, $P(D)$, and $P(H_d)$, shown schematically in Fig. 1b. The cooperative

magnetism of such a system, which generally belongs to the broad class of spin glasses [8], may be highly complex. Spin glasses contain a wide range of magnetically diluted and concentrated materials, crystalline or amorphous, site-disordered or site-ordered, but geometrically frustrated. The influence of the duality of an ordered crystal and an amorphous glass on the magnetic ground state of the TDHET "ideal" HEA is the basic question addressed in this paper.

2. Results

2.1. Magnetic measurements

Magnetic measurements were performed on a needle-shaped sample with the long axis parallel to the magnetic field, in order to minimize the demagnetization effects. The direct current (dc) magnetization M in a low magnetic field $B = 0.8$ mT, measured for the zero field cooled (zfc) and field cooled (fc) protocols, is shown in Fig. 2a (M is presented in Bohr magnetons per formula unit, i.e., per one $Tb_{0.203}Dy_{0.207}Ho_{0.203}Er_{0.197}Tm_{0.190}$ "molecule"). Upon cooling from RT, a tiny maximum is first observed at about 140 K (marked by an arrow), better visible on an expanded vertical scale in the inset of Fig. 2a. The shape of the maximum is of an antiferromagnetic (AFM)-type, but due to its smallness, it can represent only a part of the spin volume. The rest of the spins give rise to the magnetization that slowly increases upon cooling. At about 25 K, M_{zfc} and M_{fc} both start to increase strongly in a ferromagnetic (FM)-like manner. M_{fc} grows continuously and saturates at the lowest measured temperature of 1.9 K, whereas M_{zfc} exhibits a maximum at 21.5 K and then decreases toward zero in the $T \to 0$ limit. The appearance of the $M_{fc} - M_{zfc}$ difference below the M_{zfc} maximum signals nonergodicity of the spin system. In an increasing magnetic field

$B = 0.1$ T (Fig. 2b), the $M_{fc} - M_{zfc}$ difference decreases, until it vanishes in a 1 T field (Fig. 2c). In a still higher field of 5 T (Fig. 2d), the AFM-type maximum at 140 K has also disappeared and the $M(T)$ dependence indicates that the Zeeman interaction of the spins with the external field has polarized the spin system into the field direction.

The response of the spin system to an alternating current (ac) magnetic field was measured by the ac magnetic susceptibility, using the magnetic field of amplitude $B_0 = 0.65$ mT and logarithmically spaced frequencies $\nu =$ 1, 10, 100 and 1000 Hz. The real part of the ac susceptibility χ' is presented in Fig. 3a, showing two peaks. A small peak is observed at about 140 K, presented on an expanded scale in the inset. This peak is frequency independent, suggesting a thermodynamic magnetic phase transition. At about 25 K, a high-intensity peak is observed. This peak is shown on an expanded scale in Fig. 3b, revealing that it is frequency dependent and shifts to higher temperatures with increasing frequency. Such behavior is indicative of gradual freezing of spin fluctuations upon cooling with a distribution of motional frequencies. The temperature of the χ' maximum can be conveniently defined as the frequency-dependent spin freezing temperature $T_f(\nu)$. The normalized spin freezing temperature $T_f(\nu)/T_f(1\text{ Hz})$ is presented in the inset of Fig. 3b, yielding fractional shift of the freezing temperature per decade of frequency $\Gamma = \Delta T_f / T_f \Delta(\log\nu) = 5.2\times10^{-3}$, a value typically encountered in spin glasses [9].

The magnetization versus the magnetic field curves, $M(H)$, were measured for the magnetic field sweep of ± 5 T, applied after cooling the sample in zero field to the measurement temperature. The $M(H)$ curves are presented in Fig. 4 for a selected set of temperatures. The $M(H)$ curve at $T = 100$ K, typical for the upper part of the temperature range between 140 and about 30 K (denoted as range I), is shown in Fig. 4a. In the low field regime between $H = 0$ and the "critical" field H_c (marked by an arrow), the relation is linear, $M \propto H$, and we take this linear

$M(H)$ relation to be the characteristic feature that defines the range I. At H_c, the growth of the magnetization with the field becomes nonlinear and much stronger, resembling paramagnetic-like or FM-like $M(H)$ dependence. There is no hysteresis, i.e., the $M(H)$ curves for the sweeps "up" (–5 T → 5 T) and "down" (5 T → –5 T) are identical.

The $M(H)$ curve at $T = 50$ K, shown in Fig. 4b, still belongs to the range I with the linear $M \propto H$ relation at low fields. The difference to the $M(H)$ curve from Fig. 4a is that hysteresis between the sweeps up and down now appears in the region of nonlinear $M(H)$. In the sweep up, the nonlinearity sets in at the critical field H_c^{up}, whereas in the sweep down, it persists to a lower field H_c^{down}, with $H_c^{down} < H_c^{up}$ (marked by arrows). The hysteresis is observed at temperatures below 100 K and becomes larger upon lowering the temperature, i.e., the difference $H_c^{up} - H_c^{down}$ increases.

The second temperature range (range II) is entered below about 30 K. Two characteristic $M(H)$ curves in this range are shown in Fig. 4c ($T = 15$ K) and Fig. 4d ($T = 2$ K). The new features of the $M(H)$ curves in this temperature range are: (1) the linear $M \propto H$ relation in the low field region is no more present, but the magnetization grows much faster with the field in the close vicinity of $H = 0$, followed by a linear growth up to H_c^{up} or H_c^{down}; (2) the magnetization jumps at H_c^{up} and H_c^{down} are more sudden, becoming truly discontinuous at $T = 2$ K; (3) a difference between the virgin curve (obtained in the first field sweep after cooling in zero field) and the non-virgin curves (obtained in subsequent field cycles) appears and (4) small hysteresis starts to be observed also in the low-field magnetization for $0 < H < H_c^{up}, H_c^{down}$. The saturated magnetization value at $T = 2$ K amounts to $M_s = 8.2\mu_B$, which is close to the theoretical composition-averaged value $\bar{M}_s = \sum_i c_i g_i J_i \mu_B = 9\mu_B$, obtained in high fields in the $T \to 0$ limit.

Further insight into the evolution of the collective magnetic state with the temperature is presented in Fig. 5a, where the virgin $M(H)$ curves in the low-field region $0 < H < H_c^{up}$ (enclosed by a green dashed box in Fig. 4a) at temperatures below 140 K are shown on the same graph. Upon cooling, the linear $M \propto H$ relation changes into a nonlinear one in the temperature range 30–25 K, where a rapid nonlinear increase close to $H = 0$ is followed by a slower (linear-like) increase up to H_c^{up}.

The nature of the magnetic state in the TDHET HEA was also investigated by the thermoremanent magnetization (TRM) time-decay. In a TRM experiment, the sample is cooled in a field H_{fc} to a measuring temperature T_m, where the cooling is stopped and the spin system is let to age isothermally for a waiting (aging) time t_w. After t_w, the field is cut to zero and the time decay of the magnetization is monitored over macroscopic times. Upon $H_{fc} \to 0$, the reversible part of the fc magnetization M_{fc} decays to zero almost instantaneously, whereas the irreversible part (the TRM) decays in time logarithmically slow. In magnetically frustrated systems, the TRM is a fraction of M_{fc} prior to cutting H_{fc} to zero. Its magnitude varies with the temperature from a few percent at higher temperatures up to the full M_{fc} upon $T \to 0$. The M_{TRM} decay depends on the aging temperature T_m, the aging time t_w and the cooling field H_{fc}. TRM is a measure of "stiffness" of the magnetically frustrated spin system, related to the length scale of the site-averaged magnetic moment correlations $\langle \vec{J}_i(0) \cdot \vec{J}_j(r) \rangle$. This spatial correlation function defines the distance over which the spin correlations average to zero, depending on the strength of the interspin interactions. For the spin correlations that rapidly average to zero already at short distances (over a couple of interatomic spacing), the TRM is vanishing small, whereas longer spin correlations on a mesoscopic scale yield large, slowly decaying TRM.

We have measured the TRM decays at a set of temperatures T_m between 140 and 2 K. The sample was cooled always from RT to T_m in a field $\mu_0 H_{fc} = 0.2$ T, and the waiting time $t_w = 1$ h was employed. Cutting the field to zero was accomplished in about 2 min and the TRM decay was then monitored over the time t of 120 min. The TRM decay curves normalized to the fc magnetization prior to cutting the field to zero, $M_{TRM}(t)/M_{fc}$, are shown in the main panel of Fig. 6, whereas the amplitudes $M_{TRM}(0)/M_{fc}$, as a function of temperature, are shown in the inset. The TRM is nonzero only at temperatures below 25 K, where its amplitude strongly increases upon lowering the temperature and reaches $M_{TRM}(0)/M_{fc} = 0.6$ at $T = 2$ K. The time decay of the TRM is logarithmically slow. There is no TRM at temperatures above 25 K.

2.2. Specific heat

Specific heat measures the temperature-dependent changes of the internal energy E of the system, $C = \partial E/\partial T$. In an electrically conducting magnetic system like TDHET, the specific heat is a sum of the electronic, lattice and magnetic contributions, $C = C_{el} + C_{latt} + C_m$. The C_{el} and C_{latt} contributions both decrease continuously with decreasing temperature, while magnetic ordering within the spin system results in a specific heat anomaly (a peak) at the ordering temperature, originating from the magnetic specific heat C_m. At high temperatures such as RT, the lattice contribution $C_{latt} = 3R$ (where R is the gas constant) by far dominates the specific heat, whereas the electronic term $C_{el} \cong 2R(T/T_F)$, with the Fermi temperature typically in the range $T_F = 10^4$ – 10^5 K, amounts to about 1 % of the lattice term. The lattice contribution C_{latt} may be qualitatively modeled by the Debye theory [10], which becomes exact at low temperatures $T < \theta_D/50$ and at

high temperatures $T > \theta_D/2$, where θ_D is the Debye temperature. At intermediate temperatures, the departure of C_{latt} from the Debye model by up to 10 % is typical.

The total specific heat C of the TDHET in the temperature range between RT and 2 K, in magnetic fields between zero and 9 T, is shown in Fig. 7. In order to get an insight into the magnetic specific heat C_m, we plot on the same graph the theoretical Debye lattice specific heat C_{Debye} using a composition-averaged Debye temperature of the constituent elements in the metallic state, $\theta_D \approx \left(\theta_D^{Tb} + \theta_D^{Dy} + \theta_D^{Ho} + \theta_D^{Er} + \theta_D^{Tm}\right)/5 = 188$ K, where the Debye temperatures of the pure metals (all being in the interval 176–200 K) are given in Table A1. For the assumed Debye temperature, the Debye model accurately reproduces the lattice specific heat at temperatures $T > 94$ K. The theoretical Debye specific heat was scaled to match the experimental zero-field specific heat at RT. In Fig. 7, the magnetic specific heat C_m is qualitatively represented by the grey-shaded area between C and C_{Debye}.

The zero-field total specific heat C of the THDET starts to show an enhancement over the Debye model at temperatures below 200 K. Upon cooling, the enhancement rapidly increases and a rather sharp anomaly (a peak) is observed at $T \approx 137$ K, whereas below that temperature, the specific heat shows *permanent*, large enhancement over the Debye model down to the lowest temperature. At 100 K, the total specific heat C is by a factor 1.5 larger than the Debye specific heat. The permanent enhancement of C relative to C_{Debye} can be attributed to the magnetic specific heat C_m, indicating a continuous ordering within the spin system upon cooling, accompanied by a continuous heat release. At $T = 25$ K, another, small anomaly in the total specific heat appears (marked by an arrow), which is shown expanded in the inset of Fig. 7. In an increasing magnetic field up to 9 T, the anomaly at $T \approx 137$ K becomes smeared, the peak is rounded and slightly shifted to lower temperatures, but the overall enhancement of C relative to C_{Debye} remains

relatively unaffected by the field. The small anomaly at $T = 25$ K is, however, totally destroyed already by a moderate field of 0.6 T.

2.3. Magnetoresistance

The electrical resistivity ρ, measured between RT and 2 K in magnetic fields $0 - 9$ T, is described in the Appendix B and shown in Fig. B1. The resistivity is a sum of three terms, $\rho(T) = \rho_{imp} + \rho_{ph}(T) + \rho_m(T)$, where ρ_{imp} is the residual resistivity due to elastic scattering of the electrons from impurities and from lattice defects, ρ_{ph} is the contribution due to inelastic electron-phonon scattering and ρ_m is the magnetic contribution. The microscopic mechanism of ρ_m is inelastic scattering of conduction electrons by the thermally-induced magnetic excitations of the collective magnetic state. Coupling of the magnetic excitations to the conduction electrons induces electronic transitions from an occupied state $|\vec{k}\sigma\rangle$ to an unoccupied state $|\vec{k}'\sigma'\rangle$, where $\vec{k}$ is the wave vector and σ the spin of the conduction electron, which increases the resistivity. Being sensitive to the type of magnetic excitations, ρ_m is another suitable quantity to characterize the nature of the magnetic state. ρ_m is best observed in the form of magnetoresistance, $[\rho(B) - \rho(0)]/\rho(0) = \Delta\rho/\rho$. For exchange-coupled spins with parallel alignment (FM-type), the growing Zeeman interaction in an increasing external magnetic field suppresses thermally induced fluctuations of the localized 4*f* moments, resulting in a negative magnetoresistance that approaches linear variation ($\Delta\rho/\rho \propto -B$) at larger fields [11,12]. The same type of magnetoresistance is also observed in paramagnetic systems. For the spins aligned antiparallel (AFM-type), the fluctuations of spins on the sublattice parallel to the field are suppressed in the same way as in the paramagnetic and FM cases, whereas the fluctuations of spins on the antiparallel sublattice increase (the field

tries to turn over these spins). The magnetoresistance in such a case is positive and increases as $\Delta\rho/\rho \propto B^2$ at low fields [12].

The magnetoresistance of the TDHET was measured in the temperature range between 140 and 2 K by orienting the rod-shaped sample along the magnetic field (the current $I \parallel B$), in order to minimize the demagnetization effects. In Fig. 8, $\Delta\rho/\rho$ is shown at selected temperatures, which conform to the same two temperature ranges (I, II), as defined before from the $M(H)$ analysis presented in Fig. 4. The $\Delta\rho/\rho$ curves were measured separately for the sweep "up" (–9 T → 9 T) and sweep "down" (9 T → –9 T) of the magnetic field, applied after cooling the sample in zero field to the measurement temperature. The $\Delta\rho/\rho$ curve at $T = 100$ K, typical for the upper part of the temperature range I (between 140 and 100 K), is shown in Fig. 8a. In the low field regime between $B = 0$ and the critical field B_c (which is the same as the critical field $\mu_0 H_c$ in the $M(H)$ curve at 100 K of Fig. 4a), the magnetoresistance is positive and shows quadratic field dependence, $\Delta\rho/\rho \propto B^2$, typical of antiparallel-oriented, exchange-coupled spins (in Fig. 8a, the low-field magnetoresistance is enclosed by a green dashed box). At the critical field (marked by an arrow, and defined as the field where the magnetoresistance jump is the steepest), the magnetoresistance shows strong, discontinuous increase to a higher positive value, by passing through a maximum that is followed by a linear-like decrease ($\Delta\rho/\rho \propto -B$) at still higher fields, typical of parallel-oriented spins. At the critical field, the spin-flop transition obviously takes place, by polarizing the spins into the external field direction. There is no hysteresis, i.e., the $\Delta\rho/\rho$ curves for the sweeps "up" and "down" are practically the same.

The $\Delta\rho/\rho$ curve at $T = 50$ K, shown in Fig. 8b, is typical for the lower part of the temperature range I (between 100 and 30 K). In the low field region, the quadratic $\Delta\rho/\rho \propto B^2$ dependence is gradually weakened upon cooling, whereas in the high-field region, the linear

decrease ($\Delta\rho/\rho \propto -B$) is retained. The hysteresis between the sweeps up and down now appears. In the sweep up, the sharp jump of the magnetoresistance at the spin-flop transition appears at the critical field B_c^{up}, whereas in the down sweep, the jump occurs at B_c^{down}, with $B_c^{down} < B_c^{up}$. The critical fields B_c^{up} and B_c^{down} (marked by arrows in Fig. 8b) are again the same as those in the magnetization $M(H)$ curve at 50 K, shown in Fig. 4b. The hysteresis becomes larger upon lowering the temperature, so that the difference $B_c^{up} - B_c^{down}$ increases.

The $\Delta\rho/\rho$ curve at $T = 5$ K, typical of the temperature range II (below 30 K), is shown in Fig. 8c. The hysteresis between the up and down sweeps is further increased.

The temperature-dependent critical fields B_c, B_c^{up} and B_c^{down}, determined from the magnetoresistance, are shown in Fig. 8d. B_c becomes nonzero at $T \approx 140$ K and exhibits a maximum value at $T_{max} \approx 105$ K. Below T_{max}, the hysteresis starts to be observed, with $B_c^{up} > B_c^{down}$, but $B_c^{up}(T)$ and $B_c^{down}(T)$ exhibit different temperature dependencies. Below T_{max}, $B_c^{up}(T)$ first decreases upon cooling, then exhibits a shallow minimum at $T_{min} \approx$ 30–20 K and finally increases upon $T \to 0$. In contrast, the $B_c^{down}(T)$ does not show any minimum, but decreases monotonously below T_{max} down to $T \to 0$.

The evolution of the collective magnetic state with the temperature can be further elucidated by plotting the magnetoresistance curves for the sweep up in the low-field region $0 < B < B_c, B_c^{up}$ at temperatures between 140 and 2 K on the same graph (Fig. 9). The fit of the 120-K magnetoresistance with the quadratic form $\Delta\rho/\rho = \kappa B^2$ is shown in the inset (the parameter κ value is given in the Fig. 9 caption). Upon cooling from 140 K, the positive, quadratic (AFM-type) dependence gradually weakens. At temperatures below about 30 K, the magnetoresistance becomes distinctive negative, typical of paramagnetic and FM-type systems, with the largest

negative value at 25 K. The narrow temperature range around 25 K appears to be a transition region of the collective magnetic state, which changes its nature qualitatively, to be discussed next.

3. Discussion

The nature of the collective magnetic state in the TDHET "ideal" HEA is determined by an interplay of the probability distributions of the atomic moments $P(\mu)$, the exchange interaction $P(\mathcal{J})$, the anisotropy $P(D)$, and the dipolar interaction $P(H_d)$. The dipolar interaction, which leads to the domain formation in magnetic structures with a net FM moment may be, to a first approximation, ignored in an exchange-dominated system of RE elements from the heavy half of the lanthanide series without long-range FM ordering. We focus on the consequences of the distributions of the exchange interactions and the single-ion anisotropy that are both temperature dependent in the TDHET. The magnetic ground state acquired in zero and low external magnetic field depends on (1) the sign of the mean value $\bar{\mathcal{J}}$ of the exchange distribution $P(\mathcal{J})$, (2) the width $\Delta\mathcal{J}$ of the exchange distribution, with an emphasis on whether $P(\mathcal{J})$ is located entirely at positive or negative $\mathcal{J}$ values, or $P(\mathcal{J})$ extends to both sides ($\mathcal{J} > 0$ and $\mathcal{J} < 0$) and (3) the relative magnitudes of the exchange and the anisotropy terms, where we assume that both terms are significant. The different types of $P(\mathcal{J})$ distributions are depicted schematically in Fig. 10. When $\bar{\mathcal{J}} > 0$, with the entire $P(\mathcal{J})$ located at $\mathcal{J} > 0$ (Fig. 10a), the local spin ordering is ferromagnetic, but since the local easy directions wander randomly on the atomic scale or a nanoscale volume, the long-range FM order is destroyed and the magnetic structure breaks up into FM-polarized nanodomains. This is a disordered ferromagnetic state. When the $P(\mathcal{J})$ distribution extends on both $\mathcal{J} > 0$ and $\mathcal{J} < 0$ sides, but is biased towards a net positive value, $\bar{\mathcal{J}} > 0$, (Fig. 10b) the

average interaction is ferromagnetic and favors parallel ordering of the spins, but locally there are also magnetic domains with antiparallel ordering. Under the influence of the random local easy directions, the structure breaks up into magnetic nanodomains, the majority of which are FM-type and the minority are AFM-type. This type or random spin freezing is called asperomagnetism (ASPM) [13,14]. For the $P(\mathcal{J})$ located entirely on the $\mathcal{J} < 0$ side, the average exchange is antiferromagnetic, $\bar{\mathcal{J}} < 0$ (Fig. 10c), and spins freeze into a random, noncollinear ground state with antiparallel nearest-neighbor ordering and a high degree of degeneracy, where many different spin configurations have almost the same energy. This kind of random spin freezing is known as speromagnetism (SPM) [13,14]. Speromagnetism and asperomagnetism are both encountered in amorphous magnets, where no crystal lattice exists.

Speromagnetism and asperomagnetism are distinguished by the length scale over which the spin correlations average to zero. In a speromagnet, site-averaged spin correlations $\langle \vec{J}_i(0) \cdot \vec{J}_j(r) \rangle$ are negative at the nearest-neighbor distance, but rapidly average to zero over a couple of interatomic distances. In an asperomagnet, the correlations are ferromagnetic and average to zero on a much longer, mesoscopic spatial scale.

A special situation is encountered when the $P(\mathcal{J})$ distribution is symmetric and centered at zero, so that $\bar{\mathcal{J}} = 0$ (Fig. 10d). In this case, the average exchange interaction is zero and spins freeze individually in random directions below the spin freezing temperature T_f. This is a theoretical definition a spin glass (SG) state [8].

The different sorts of magnetic ordering described above are best distinguished by their magnetization curves, shown schematically in Fig. 10. The $M(H)$ curve of a disordered ferromagnet is shown in Fig. 10a. The $M(H)$ dependence can be modeled by a Langevin function $L(x)$ with $x = g\mu_B J\mu_0 H/(k_B T)$, which assumes that classical moments $\mu = g\mu_B J$ can be

continuously aligned in the field and the angular momentum J can assume any value ($J \to \infty$), accounting for the large effective group spins of the FM domains. For large x, the Langevin function saturates to a constant (horizontal) plateau. For an asperomagnet with the $P(\mathcal{J})$ shown in Fig. 10b, the magnetization curve can be described by a sum of the Langevin function that accounts for the FM domains, $M_{FM} = M_0 L(x)$, and a linear function that accounts for the AFM domains, $M_{AFM} = kH$, where k represents the AFM susceptibility. At large fields, the magnetization of an asperomagnet, $M_{ASPM} = M_0 L(x) + kH$, saturates to a linear, inclined line with the slope k (Fig. 10b). The magnetization curve of a speromagnet with the $P(\mathcal{J})$ shown in Fig. 10c is linear, $M_{SPM} = kH$. For a spin-glass $P(\mathcal{J})$ of Fig. 10d, the $M(H)$ relation is also a sum of the linear term, corresponding to the portion of $P(\mathcal{J})$ on the negative side $\mathcal{J} < 0$, whereas the portion of $P(\mathcal{J})$ on the positive side $\mathcal{J} > 0$ contributes a magnetization term with a field dependence stronger than linear. The dependence can still be of a Langevin-type, but since the average exchange interaction in a spin glass is zero, $\bar{\mathcal{J}} = 0$, the effective angular momentum J will be smaller than for the asperomagnet. The spin glass-type magnetization curve $M_{SG} = M_0 L(x) + kH$ is shown in Fig. 10d.

In a sufficiently large external magnetic field, the Zeeman interaction wins over the exchange and the anisotropy, which destroys the collective magnetic states (SPM, ASPM, SG). The stable configuration is then an array of moments $g_i \mu_B J_i$ pointing along the field direction. In the TDHET, the polarization of spins in the field up sweep starts at the critical field B_c^{up}, whereas in the field down sweep, depolarization is completed at B_c^{down}, with $B_c^{down} < B_c^{up}$. At temperatures above 100 K, thermal fluctuations cause the two critical fields to be equal. The origin of this hysteresis in the high-field regime is a myriad of degenerate spin configurations that exist in the SPM, ASPM and SG states. The hysteresis can be understood in the mean-field picture [15].

We assume that five different types of RE ions with the angular momenta $\vec{J}_m$ ($m = 1 - 5$ referring to Tb, Dy, Ho, Er and Tm) are randomly distributed over the lattice sites *i*. The mean-field Hamiltonian of an ion *m* located at the site *i* consists of the CF, the exchange and the Zeeman terms

$$\mathcal{H}_m^{MF}(i) = \mathcal{H}_{cf}^m(\vec{J}_{mi}) - \vec{J}_{mi} \cdot \vec{b}_{mi}^{eff}. \quad (1)$$

The effective field $\vec{b}_{mi}^{eff}$ has two contributions, one from the external field $\vec{B}$ and the other is the exchange field

$$\vec{b}_{mi}^{eff} = g_m \mu_B \vec{B} + \sum_{n,j}(g_m - 1)(g_n - 1)\mathcal{J}_{mn}(ij)c_{n,j}\langle\vec{J}_{nj}\rangle. \quad (2)$$

The summation j runs over all lattice sites surrounding the site i, whereas the summation n goes over all types (1 – 5) of the RE ions. $\mathcal{J}_{mn}(ij)$ is the RKKY coupling constant between the m-type ion located at the site *i* and the n-type ion located at j. The bracket $\langle ... \rangle$ denotes the expectation (mean) value of the angular momentum operator and $c_{n,j}$ denotes a variable, which is 1 if the ion on site j is of type n, and 0 if it is other type than n. The configurational average $\langle c_{n,j}\rangle_{conf} = c_n$ gives the atomic concentration of the n-type ions in the HEA mixture.

The hysteresis originates from the exchange field. Starting the field up sweep from $\vec{B} = 0$, the variables $\langle\vec{J}_{nj}\rangle$ are initially oriented in many directions in the SPM and ASPM states, so that their weighted sum in the second term of Eq. (2), representing the exchange field, is small. When the external field starts to polarize the spins for $B > B_c^{up}$, the $\langle\vec{J}_{nj}\rangle$ rotate into the field direction, the exchange field grows and reaches a saturated value when all $\langle\vec{J}_{nj}\rangle$ are coerced with the field. In the subsequent field down sweep, the moments remain coerced due to high degeneracy of the spin configurations, so that the exchange field in the down sweep is higher than in the preceding up sweep. Depolarization of the coerced spins into the SPM or ASPM configurations consequently

happens in a lower external field, yielding the hysteresis $B_c^{down} < B_c^{up}$. The dipolar fields, which were neglected so far, add to this hysteresis.

The temperature-dependent cooperative magnetic ordering in the TDHET HEA in zero and low magnetic field can be described by the following sequence of collective magnetic states upon cooling from RT. At $T \approx 140$ K, a paramagnetic to speromagnetic transition takes place. Due to the distribution of the RKKY exchange coupling constants, local domains enriched in Tb and Dy with the strongest coupling constants order first in an AFM-type spin alignment. This results in a small peak in the dc susceptibility at about 140 K. A tiny peak in the ac susceptibility at the same temperature, which is frequency independent, reveals a thermodynamic phase transition. The magnetic specific heat also shows a peak at the para-to-SPM phase transition. Upon lowering the temperature, the domains containing also other elements (Ho, Er, Tm) order magnetically, but due to the random distribution of the elements and the corresponding exchange coupling constants, magnetic ordering is a continuous process, which results in a large, continuous magnetic specific heat contribution. The magnetic ground state in the entire temperature range between 140 and 30 K (corresponding to the range I) is ultimately speromagnetic, as supported by the linear $M(H)$ relation (the fit at 50 K is shown in Fig. 5b), small dc magnetization and positive, quadratic magnetoresistance, $\Delta\rho/\rho \propto B^2$, all resulting from the antiparallel local spin alignment. The very short site-averaged spin correlations of the SPM state are reflected in the vanishing TRM.

The low-temperature collective magnetic state below about 20 K is asperomagnetic. The fc dc magnetization is large and grows strongly upon cooling, whereas the zfc magnetization exhibits a cusp and decreases towards zero upon $T \to 0$, as typical for a disordered FM-type system with a random distribution of local anisotropies. The ASPM state is corroborated by the ASPM-

type $M(H)$ relation (the fit at 15 K is shown in Fig. 5b), the negative magnetoresistance $\Delta\rho/\rho \propto -B$, whereas the long site-averaged spin correlations are reflected in a large TRM.

Since, upon cooling, the high-temperature SPM state with the $P(\mathcal{J})$ distribution biased toward a net negative value, $\bar{\mathcal{J}} < 0$, evolves continuously into the ASPM state with the $P(\mathcal{J})$ distribution biased toward a net positive value, $\bar{\mathcal{J}} > 0$, it must pass through the $\bar{\mathcal{J}} = 0$ condition at a certain temperature. The SPM and the ASPM states should therefore necessarily be separated by a SG state within a narrow temperature interval. In the TDHET, the SG state is entered in the temperature range between 30 and 20 K. The SG state is signaled by a large, frequency-dependent peak in the ac susceptibility at 25 K with a shift of the freezing temperature per decade of frequency Γ typical of spin glasses. The $M(H)$ relation is also typical of a SG state (the fit at 30 K is presented in Fig. 5b), whereas the negative, paramagnetic-type low-field magnetoresistance, which is most negative at 25 K (Fig. 9) reflects the zero average exchange interaction ($\bar{\mathcal{J}} = 0$) in a spin glass. The weakened interspin interactions are also mirrored in the field-dependence of the tiny maximum in the magnetic specific heat at 25 K, which is totally destroyed by an already small magnetic field of 0.6 T.

A continuous, monotonous shift of the $P(\mathcal{J})$ distribution on the $\mathcal{J}$ axis upon cooling from the high-temperature SPM-type with $\bar{\mathcal{J}} < 0$, through the SG-type with $\bar{\mathcal{J}} = 0$, to the low-temperature ASPM-type with $\bar{\mathcal{J}} > 0$ is also reflected in the temperature dependence of the "up" critical field $B_c^{up}(T)$, shown in Fig. 8d. In the SPM state, a continuous shift of $\bar{\mathcal{J}} < 0$ in the direction $\bar{\mathcal{J}} \to 0$ results in a continuous decrease of B_c^{up} upon cooling, reflecting the fact that at lower temperatures, smaller external magnetic field is already sufficient to start polarizing the exchange coupled spins with a weakened exchange interactions. Upon crossing $\bar{\mathcal{J}} = 0$ (in the SG state), B_c^{up} reaches a minimum value, whereas upon further cooling into the ASPM state, the $\bar{\mathcal{J}} >$

0 shifts monotonously away from $\bar{J} = 0$, causing B_c^{up} to grow again due to strengthening of the exchange interactions.

The observed temperature evolution of the collective magnetic ground state in the TDHET HEA in the sequence SPM→SG→ASPM is a result of a compromise between the temperature-dependent competing magnetic interactions to which the magnetic moments are subjected. The phase transitions originate from the temperature dependence of various terms in the Hamiltonian, which can be qualitatively discussed in the mean-field picture using Eqs. (1) and (2). The first term in the mean-field Hamiltonian is the CF interaction, where the interaction energy is $\varepsilon_{cf} = \int e\rho_{4f}(\vec{r})\varphi_{cf}(\vec{r})d^3r$. Here e is the electron charge, ρ_{4f} is the $4f$ electron density and $\varphi_{cf}(\vec{r})$ is the electrostatic potential created by the charge distribution of the crystal at the RE site. The $4f$ charge density can be expanded in spherical harmonics, allowing to express the CF interaction in terms of 2^n-pole moments Q_n of the charge distribution, where n is even (e.g., Q_2 is the electric quadrupole moment). According to Stevens, the CF interaction can then be expressed in terms of angular momentum operators (by using the Wigner-Eckart theorem), yielding the CF Hamiltonian of the ion at the site i for the hexagonal lattice symmetry [16]

$$\mathcal{H}_{cf}(i) = \sum_{n=2,4,6} B_n^0 O_n^0(\vec{J}_i) + B_6^6 O_6^6(\vec{J}_i), \qquad (3)$$

where B_n^m are crystal-field parameters and $O_n^m(\vec{J})$ are Stevens operators. The crystal-field parameters are written as $B_n^m = \theta_n \langle r_{4f}^n \rangle A_n^m$, where A_n^m describe spatial variation of the crystal potential φ_{cf} (e.g., A_2^0 is the electric field gradient at the RE site due to the crystal charges), $\langle r_{4f}^n \rangle$ is an average of r^n over the $4f$ radial wave function and θ_n is a constant, different for each RE element, which is proportional to the 2^n-pole moment Q_n. While the parameters A_n^m change little with the temperature, the temperature dependence of the multipole moments Q_n is generally strong, giving rise to a pronounced temperature dependence of the anisotropy forces. The

temperature dependence of the moments Q_n can be evaluated from the thermodynamic averages $\langle O_n^0 \rangle$.

The temperature-dependence of the exchange interactions originates from the variables $\langle \vec{J}_{nj} \rangle$, where the temperature-induced changes in the magnitude and orientation of the moments $g_n \mu_B \langle \vec{J}_{nj} \rangle$ alter the band structure of the conduction electrons, which in turn modifies the RKKY exchange constants $\mathcal{J}_{mn}(ij)$. Strong temperature dependence of the RKKY exchange interaction is a known phenomenon in pure RE metals from the heavy half of the lanthanide series [15], being responsible for the phase transition from the modulated AFM to the FM state in the metallic state of all five RE elements that constitute the TDHET HEA (the Néel temperatures T_N and the Curie temperatures T_C of the Tb, Dy, Ho, Er and Tm metals are given in Table A1). In the pure RE metals, the Fourier transform $\mathcal{J}(\vec{q})$ of the exchange constant defined via the relation $\mathcal{J}(\vec{q}) = \sum_j \mathcal{J}(ij) \exp\{-i\vec{q} \cdot (\vec{R}_i - \vec{R}_j)\}$ (where $\vec{R}_i$ are Bravais lattice vectors) exhibits a maximum at a non-zero wave vector $\vec{q}$, which is responsible for stabilizing periodic magnetic structures at high temperatures in the hcp lattice (a basal-plane helical AFM structure in the Tb, Dy and Ho metals and a longitudinal-wave AFM structure in Er and Tm [17]). The peak in $\mathcal{J}(\vec{q})$ is a consequence of the specific form of the Fermi surface [18]. The magnitude of the peak increases monotonically with the atomic number, being the smallest in Tb and the largest in Tm. Due to the temperature-induced changes of the conduction-electron band structure, the regions of the Fermi surface responsible for the peak in $\mathcal{J}(\vec{q})$ are severely modified [19]. As a result, $\mathcal{J}(\vec{q})$ changes continuously with the temperature in a way that the position of the peak moves in the direction $\vec{q} \to 0$ and its magnitude is reduced. The competition of the temperature-dependent exchange and the anisotropy forces then yields the phase transition from the modulated AFM ($\vec{q} \neq 0$) to the low-temperature FM ($\vec{q} = 0$) state.

The temperature evolution of the exchange coupling constant in the heavy RE metals, responsible for the AFM→FM transition, is a band-structure effect, closely linked with the crystallinity of the spin system. The continuous, temperature-dependent shift of the $P(\mathcal{J})$ distribution on the $\mathcal{J}$ axis in the TDHET HEA, responsible for the SPM→SG→ASPM transition, is completely analogous. This analogy suggests that the effect can also be attributed to the temperature-dependent band-structure changes, linked with the crystallinity of the TDHET HEA. The shift of the $P(\mathcal{J})$ from $\bar{\mathcal{J}} < 0$ through $\bar{\mathcal{J}} = 0$ to $\bar{\mathcal{J}} > 0$ is thus an effect related to the crystal lattice, which the TDHET "metallic glass on an ordered lattice" shares with the pure, chemically ordered RE crystalline systems. The probability distributions of the atomic moments $P(\mu)$, the exchange interactions $P(\mathcal{J})$, the anisotropy $P(D)$, and the dipolar interactions $P(H_d)$ are, on the other hand, a consequence of the chemical disorder, a property that the TDHET HEA shares with the amorphous magnets (metallic glasses). Both features, the topologically ordered lattice and the amorphous-type chemical disorder thus essentially determine the collective magnetic state of an ideal, RE-based HEA. Comparing the magnetic states of the heavy RE metals and the TDHET HEA, the following analogy is evident. The high-temperature state in the RE metals is AFM, whereas in the TDHET it is replaced by a speromagnetic state, which can be viewed as a strongly disordered variant of the AFM state. Likewise, the low-temperature FM state in the RE metals is replaced in the TDHET by an asperomagnetic state, a strongly disordered variant of the FM state. During continuous evolution of the SPM state into the ASPM state by lowering the temperature, the two states are necessarily separated by a spin glass state within a narrow temperature interval. The appearance of the intermediate SG state in a RE-based HEA has no analogy in the pure RE metals.

We comment why the speromagnetism and asperomagnetism were not reported for the previously investigated RE-based HEAs Gd-Tb-Dy-Ho-Y [2], Gd-Tb-Dy-Ho-Lu [3] and Gd-Tb-Dy-Ho-Ce [4]. The pair mixing enthalpies of all the employed RE elements are zero, assuring random mixing in the solid solution. The atomic-size-difference parameter $\delta \approx 1$ % is small in all cases, so that the lattice distortions are small. According to these criteria, the above HEAs can also be considered to belong to the class of "ideal" HEAs. However, there are important differences to the Tb-Dy-Ho-Er-Tm HEA. The Gd-Tb-Dy-Ho-Y and Gd-Tb-Dy-Ho-Lu HEAs, which crystallize in the hcp structure, contain one nonmagnetic element each (Y or Lu), whereas the Gd ion possesses a spherically symmetric 4*f* charge cloud, implying zero single-ion magnetocrystalline anisotropy. The remaining ions Tb, Dy and Ho all possess an oblate 4*f* charge cloud, so that the CF interaction aligns their moments in the hexagonal plane, giving rise to planar magnetic structures. In the Gd-Tb-Dy-Ho-Y and Gd-Tb-Dy-Ho-Lu HEAs, only 60 % of the ions possess the CF anisotropy and the probability distribution of local anisotropies $P(D)$ is not of an amorphous-magnet type. The situation is similar in the Gd-Tb-Dy-Ho-Ce HEA, where Ce is also an oblate ion, but there is an additional complication that the pure Ce metal does not crystallize in the hcp structure, which further compromises the ideality of this HEA. The Gd-Tb-Dy-Ho-Ce HEA was found to be structurally a two-phase compound, consisting of the hcp majority phase and a rhombohedral minority phase. In contrast, the Tb-Dy-Ho-Er-Tm hexagonal HEA that contains also the prolate ions Er and Tm is a true random-anisotropy system, possessing 100 % ions with non-zero CF anisotropy and the magnetic moments are directed in the entire space, giving rise to the speromagnetic and asperomagnetic structures.

The above results on the speromagnetism and asperomagnetism being the collective magnetic states of an ideal HEA is valid for a RE-based system and cannot be directly generalized

to magnetic HEAs composed of the 3*d* magnetic transition elements Fe, Co, Ni, Cr and Mn. While the local random anisotropy is usually sufficient to pin the local magnetic moment's direction in 4*f* alloys, it is generally insufficient to pin it in 3*d* alloys. The assumption of local easy directions that wander randomly on a nanoscale is consequently not justified, so that the 3*d* HEAs cannot be considered as random local anisotropy systems with a continuous distribution of local anisotropies $P(D)$. The 3*d* ions can also have delocalized *d* electrons, so that the moments may not be localized as they are in the case of 4*f* ions. Lastly, the pair mixing enthalpies between the magnetic 3*d* transition elements are generally nonzero (with the exception of Co-Ni and Fe-Mn pairs), so that random mixing of the elements on the crystal lattice is compromised and local preferential chemical environments are formed on a nanoscale [20-22]. There is no unique description of the collective magnetic state in a "regular" HEAs based on the Fe, Co, Ni, Cr and Mn [23-28], but the magnetic state depends sensitively on the choice of the elements (where Fe, Co and Ni promote ferromagnetism, whereas Cr and Mn are AFM), their concentrations and the possible addition of other elements (e.g., Al, Zr).

4. Conclusions

The Tb-Dy-Ho-Er-Tm HEA is a physical realization of an ideal HEA with completely random mixing of the elements on a practically undistorted hexagonal lattice. It represents a magnetically concentrated system with all lattice sites occupied by localized magnetic moments and containing randomness and frustration due to chemical disorder, sharing properties of an ordered crystal and an amorphous glass. We have studied the influence of this crystal-glass duality on the collective magnetic state and found that the state is temperature-dependent, forming a speromagnetic state in

the temperature range between about 140 and 30 K and an asperomagnetic state below 20 K. In the intermediate temperature range between 30 and 20 K, a spin glass state is formed, representing a transition state between the SPM and the ASPM states. The observed temperature evolution of the magnetic ground state in the TDHET HEA upon cooling in the sequence SPM→SG→ASPM is a result of temperature-dependent, competing magnetic interactions. The distribution of the exchange interactions $P(\mathcal{J})$ shifts continuously on the $\mathcal{J}$ axis from the high-temperature SPM-type with the average interaction biased towards a net negative value, $\bar{\mathcal{J}} < 0$, through the SG-type with $\bar{\mathcal{J}} = 0$, to the low-temperature ASPM-type with $\bar{\mathcal{J}} > 0$. This shift is a band-structure effect, closely linked with the crystallinity of the spin system, which the TDHET HEA shares with the topologically ordered crystals. The probability distributions of the atomic moments $P(\mu)$, the exchange interactions $P(\mathcal{J})$, the magnetocrystalline anisotropy $P(D)$ and the dipolar interactions $P(H_d)$ are, on the other hand, a consequence of chemical disorder, a property that the TDHET HEA shares with the amorphous magnets. Both features, the topologically ordered lattice and the amorphous-type chemical disorder essentially determine the magnetic state of an ideal, RE-based HEA.

Acknowledgments

Slovenian authors acknowledge the financial support from the Slovenian Research Agency (research core funding No. P1-0125). MF acknowledges financial support from the German Research foundation (DFG) under grant No. FE 571/4 within the priority program SPP2006 “Compositionally Complex Alloys – High Entropy Alloys (CCA-HEA)”.

Declarations of interest: none.

Appendix A: Material and methods

The Tb-Dy-Ho-Er-Tm polygrain material was prepared in a high-frequency levitation furnace under 1 bar Ar atmosphere. The details of preparation can be found elsewhere [1]. The XRD pattern, obtained by a PANalytical X'Pert PRO MPD diffractometer, is shown in Fig. A1. The material is single-phase and all peaks could be indexed using a unit cell of a hcp structure with the lattice parameters a = 3.582(2) Å and c = 5.632(3) Å and space group $P6_3/mmc$. Miller indices hkl are written in parentheses above the peaks. The experimentally determined unit cell parameters match well to the composition-averaged theoretical values for this alloy $\bar{a}$ = 3.575 Å and $\bar{c}$ = 5.622 Å (Table A1). Closer inspection of the diffraction pattern reveal that the $00l$ peaks are somewhat broader than the $hk0$ ones. Such anisotropic peak broadening indicates that the crystallographic order along the hexagonal c direction is not as good as in the hexagonal basal (a, b) plane . Taking into account that the peak broadening can be caused by either short coherently scattering domains or by microstrain or by both, we took the limiting cases (pure size broadening and pure microstrain broadening) to estimate the ranges of the size-strain parameters, using the Scherrer's formula. Using the "pure size" approach, we found that the coherently scattering domains in the (a, b) plane are about 100 nm long, while they are 3 times shorter along the c direction. The "pure strain" approach led to the deformation of the lattice parameter by about 0.2 % in the (a, b) plane and 0.3 % along the c direction. Most likely, the anisotropic broadening of the XRD peaks is due to a combination of the size and the strain effects.

A SEM backscattered-electron image of the Tb-Dy-Ho-Er-Tm sample is shown in Fig. A2. Polycrystalline morphology of the material with very large grains is evident, with some of the grains approaching mm size. The microstructure of differently oriented grains is observed due to channeling contrast, which reflects their good crystallinity. The EDS-determined composition was $Tb_{20.3}Dy_{20.7}Ho_{20.3}Er_{19.7}Tb_{19.0}$ (in at. %) with about 0.5 % uncertainty for each element, so that the composition is close to the nominal equiatomic target.

Magnetic measurements were conducted by a Quantum Design MPMS XL-5 SQUID magnetometer equipped with a 5 T magnet, whereas the specific heat and the magnetoresistance were measured by a Quantum Design Physical Property Measurement System (PPMS 9 T), equipped with a 9 T magnet, both apparatus operating down to 1.9 K temperature.

Appendix B: Electrical resistivity

The temperature-dependent electrical resistivity of the TDHET in magnetic fields $0-9$ T is shown in Fig. B1. The $\rho(T)$ dependence is metallic with a positive temperature coefficient. The RT value of the zero-field resistivity is $\rho_{300K} = 107$ μΩcm and the low-temperature residual value is $\rho_{2K} = 32$ μΩcm. The resistivity shows interesting behavior in the magnetic field, where the zero-field resistivity is enhanced over the 9-T resistivity below about 140 K. The resistivity at intermediate fields is also enhanced relative to the 9-T resistivity, but the enhancement does not change monotonously with the field and is also temperature dependent (inset in Fig. B1). The dependence of the resistivity on the magnetic field is best observed in the magnetoresistance, as discussed in the paragraph *2.3.* of the main paper.

Table A1. Properties of pure RE metals and the $Tb_{20.3}Dy_{20.7}Ho_{20.3}Er_{19.7}Tb_{19.0}$ HEA (the structural parameters, the Landé g-factor, the angular momentum J, the Néel temperature T_N, the Curie temperature T_C and the Debye temperature θ_D) [15]. Theoretical values for the HEA are composition-averaged values, $\bar{Y} = \sum_i c_i Y_i$, where c_i is the molar concentration of the element i.

	Tb	Dy	Ho	Er	Tm	HEA exp.	HEA theory
Structure (300 K)	hcp	hcp	hcp	hcp	hcp	hcp	
a (Å)	3.606	3.592	3.578	3.559	3.538	3.582	3.575
c (Å)	5.697	5.650	5.618	5.585	5.554	5.632	5.622
Metallic radius r (Å) [29]	1.773	1.781	1.762	1.761	1.759		
g	3/2	4/3	5/4	6/5	7/6		
J	6	15/2	8	15/2	6		
T_N (K)	230	179	132	85	58		
T_C (K)	220	89	20	20	32		
θ_D (K)	176	183	190	188	200		188

References

[1] M. Feuerbacher, M. Heidelmann, and C. Thomas, Mat. Res. Lett. 3, 1 (2014).

[2] J. Lužnik, P. Koželj, S. Vrtnik, A. Jelen, Z. Jagličić, A. Meden, M. Feuerbacher, and J. Dolinšek, Phys. Rev. B **92**, 224201 (2015).

[3] S. Vrtnik, J. Lužnik, P. Koželj, A. Jelen, J. Luzar, M. Krnel, Z. Jagličić, A. Meden, M. Feuerbacher, and J. Dolinšek, Intermetallics **105**, 163 (2019).

[4] S. Vrtnik, J. Lužnik, P. Koželj, A. Jelen, J. Luzar, Z. Jagličić, A. Meden, M. Feuerbacher, and J. Dolinšek, J. Alloys Compd. **742**, 877 (2018).

[5] W. Hume-Rothery, Factors affecting the stability of metallic phases. In: *Phase Stability in Metals and Alloys*, P. S. Rudman, J. Stringer, R. I. Jaffee (Eds.) (McGraw-Hill, New York, 1967), pp. 3-23.

[6] A. Takeuchi and A. Inoue, Mat. Trans. **46**, 2817 (2005).

[7] Y. Hirayama, T. Nakagawa, and T. A. Yamamoto, Solid State Commun. **151**, 1602 (2011).

[8] K. Binder and A. P. Young, Rev. Mod. Phys. **58** ,801 (1986).

[9] J. A. Mydosh, *Spin Glasses: An Experimental Introduction* (Taylor & Francis, London, 1993), p. 67.

[10] See, e.g., A. Tari, *The Specific Heat of Matter at Low Temperatures* (Imperial College Press, London, 2003), p. 26.

[11] H. Yamada and S. Takada, Prog. Theor. Phys. **48**, 1828 (1972).

[12] H. Yamada and S. Takada, J. Phys. Soc. Jpn. **34**, 51 (1973).

[13] J. M. D. Coey, *Magnetism and Magnetic Materials* (Cambridge University Press, Cambridge, 2010), pp. 209–218.

[14] R. C. O'Handley, *Modern Magnetic Materials: Principles and Applications* (Wiley, New York, 1999), pp 391–410.

[15] J. Jensen and A. R. Mackintosh, *Rare Earth Magnetism* (Clarendon Press, Oxford, 1991), and references therein.

[16] E. Segal and W. E. Wallace, *Rare Earth Intermetallics* (Academic Press, New York, 1973).

[17] W. C. Koehler, Magnetic Structures of rare Earth Metals and Alloys. In: *Magnetic Properties of Rare Earth Metals*, R. J. Elliott (Eds.) (Plenum Press, London, 1972,) p. 81.

[18] R. W. Williams and A. R. Mackintosh, Phys. Rev. **168**, 679 (1968).

[19] R. E. Watson, A. J. Freeman, and J. P. Dimmock, Phys. Rev. **167**, 497 (1968).

[20] L. J. Santodonato, Y. Zhang, M. Feygenson, C. M. Parish, M. C. Gao, R. J. K. Weber, J. C. Neuefeind, Z. Tang, and P. K. Liaw, Nat. Commun. **6**, 5964 (2015).

[21] S. Vrtnik, P. Koželj, A. Meden, S. Maiti, W. Steurer, M. Feuerbacher, and J. Dolinšek, J. Alloys Compd. **695**, 3530 (2017).

[22] P. Koželj, S. Vrtnik, A. Jelen, M. Krnel, D. Gačnik, G. Dražić, A. Meden, M. Wencka, D. Jezeršek, J. Leskovec *et al*., Adv. Eng. Mater. 1801055 (2019), DOI: 10.1002/adem.201801055.

[23] See, for a review, B. S. Murthy, J. W. Yeh, and S. Ranganathan, *High-Entropy Alloys* (Elsevier, Amsterdam, 2014), pp. 154-155.

[24] See, for a review, J. W. Yeh, S.-K. Chen, H. C. Shih, Y. Zhang, and T. T. Zuo, Functional properties. In: *High-Entropy Alloys: Fundamentals and Applications*, M. C. Gao, J. W. Yeh, P. K. Liaw, Y. Zhang (Eds.) (Springer International Publishing Switzerland, 2016), pp. 243-248.

[25] Y. Zhang, T. T. Zuo, Y. Q. Cheng, and P. K. Liaw, Sci. Rep. **3**, 1455 (2013).

[26] P. F. Yu, L. J. Zhang, H. Cheng, H. Zhang, M. Z. Ma, Y. C. Li, G. Li, and P. K. Liaw, Intermetallics **70**, 82 (2016).

[27] P. Li, A. Wang, and C. T. Liu, J. Alloys. Compd. **694**, 55 (2017).

[28] M. H. Tsai, Entropy **15**, 5338 (2013).

[29] N. N. Greenwood, A. Earnshaw, *Chemistry of Elements*, 2nd ed. (Butterworth-Heinemann Elsevier, Oxford, 1997).

Figure captions

Fig. 1. (a) The de Gennes factor G_{ij} normalized to G_{TbTb} for all fifteen atomic pairs of the elements Tb, Dy, Ho, Er and Tm. The inset shows the first coordination shell of a given atom in the hcp structure of $P6_3/mmc$ symmetry, by assuming random mixing of the five elements. There are two slightly different distances between the central atom and the atoms of the first coordination shell, which for the TDHET unit cell amount to $r_1 = 3.582$ Å and $r_2 = 3.494$ Å. **(b)** A schematic presentation of the probability distributions of the atomic moments $P(\mu)$, the exchange interactions $P(\mathcal{J})$, the anisotropies $P(D)$ and the dipolar interactions $P(H_d)$ in the TDHET "ideal" HEA.

Fig. 2. Temperature-dependent zfc and fc dc magnetizations of the TDHET HEA between RT and 2 K in magnetic fields **(a)** $B = 0.8$ mT, **(b)** 0.1 T, **(c)** 1 T, and **(d)** 5 T. "f.u." denotes formula unit, i.e., one $Tb_{0.203}Dy_{0.207}Ho_{0.203}Er_{0.197}Tm_{0.190}$ "molecule".

Fig. 3. (a) Real part χ' of the ac magnetic susceptibility of the TDHET at frequencies $\nu = 1$, 10, 100 and 1000 Hz. The inset shows χ' in the range of the magnetic phase transition at 140 K on an expanded temperature scale (the curves for all frequencies perfectly overlap). **(b)** Low-temperature χ', showing a frequency-dependent peak at $T \approx 25$ K. The temperature of the peak maximum is associated with the frequency-dependent spin freezing temperature $T_f(\nu)$ (marked by an arrow on the 1-Hz curve). The inset shows the normalized freezing temperature $T_f(\nu)/T_f(1\ Hz)$.

Fig. 4. The magnetization versus the magnetic field curves of the TDHET HEA. **(a)** $M(H)$ at $T =$ 100 K, typical for the upper part (140 – 100 K) of the temperature region I. Vertical arrow marks

the critical field H_c, where the linear $M \propto H$ relation (enclosed in a green dashed box) changes into a stronger, nonlinear one. **(b)** $M(H)$ at $T = 50$ K, typical for the lower part (100 – 30 K) of the temperature region I. In the sweep up, the $M \propto H$ linearity is present in the field range $0 < H < H_c^{up}$, whereas in the down sweep, the linearity is confined to a smaller range $0 < H < H_c^{down}$, with $H_c^{up} > H_c^{down}$. In the panels **(c)** and **(d)**, the $M(H)$ curves at $T = 15$ K and $T = 2$ K are shown, respectively, both being typical for the low-temperature region II. The linearity $M \propto H$ in the low field region is no more present and there is a difference between the virgin and the non-virgin curves. The abbreviation SPM denotes speromagnetism and ASPM stands for asperomagnetism.

Fig. 5. (a) Virgin $M(H)$ curves in the low-field region $0 < H < H_c^{up}$ (marked by a green dashed box in Fig. 4a) at temperatures below 140 K. Neighboring experimental points are connected by straight lines. **(b)** Typical speromagnetic (SPM), spin glass (SG) and asperomagnetic (ASPM) $M(H)$ curves at the temperatures 50, 30 and 15 K, respectively. Solid curves are the theoretical fits. The SPM curve was reproduced by $M_{SPM} = k\mu_0 H$ with $k = 0.66\ \mu_B$/f.u. T^{-1}; the ASPM curve was reproduced by $M_{ASPM} = M_0 L(\mu\mu_0 H/k_B T) + k\mu_0 H$ with $\mu = 330\ \mu_B$, $M_0 = 1.23\ \mu_B$/f.u. and $k = 0.69\ \mu_B$/f.u. T^{-1}, whereas the SG curve was reproduced by the same formula as the ASPM curve, but with different fit parameter values $\mu = 142\ \mu_B$, $M_0 = 0.76\ \mu_B$/f.u. and $k = 0.66\ \mu_B$/f.u. T^{-1}.

Fig. 6. The normalized TRM time-decay curves $M_{TRM}(t)/M_{fc}$ at a selected set of temperatures between 140 and 2 K. The inset shows the amplitudes $M_{TRM}(0)/M_{fc}$ as a function of temperature.

Fig. 7. Specific heat C of the TDHET in the temperature range between RT and 2 K, in magnetic fields between zero and 9 T. The theoretical Debye lattice specific heat C_{Debye}, using a composition-averaged Debye temperature of the constituent elements, $\theta_D = 188$ K, is shown by a dashed curve. The magnetic specific heat C_m is qualitatively represented by the grey-shaded area between C and C_{Debye}. The arrow marks the additional, small anomaly at 25 K, which is shown expanded in the inset, as a function of the magnetic field.

Fig. 8. The magnetoresistance curves of the TDHET. **(a)** $\Delta\rho/\rho$ at $T = 100$ K, typical for the upper part (140 – 100 K) of the temperature range I. Vertical arrow marks the critical field B_c, where the spin-flop transition takes place. **(b)** $\Delta\rho/\rho$ at $T = 50$ K, typical for the lower part (100 – 30 K) of the temperature range I. In the sweep up, the spin-flop transition appears at the critical field B_c^{up}, whereas in the down sweep, it occurs at B_c^{down} (both critical fields are marked by arrows). **(c)** $\Delta\rho/\rho$ at $T = 5$ K, typical of the temperature range II. **(d)** Temperature-dependent critical fields B_c, B_c^{up} and B_c^{down}, determined from the magnetoresistance. The speromagnetic (SPM), the spin glass (SG) and the asperomagnetic (ASPM) states are delimited by vertical dashed lines based on the $B_c^{up}(T)$ critical field.

Fig. 9. The magnetoresistance curves for the up sweep in the low-field region $0 < B < B_c, B_c^{up}$ at selected temperatures between 138 and 2 K. The inset shows the speromagnetic-type magnetoresistance at 120 K. Solid curve is the fit with the quadratic form $\Delta\rho/\rho = \kappa B^2$, using the fit parameter $\kappa = 0.12$ T^{-2}.

Fig. 10. A schematic presentation of different sorts of magnetic ordering based on the distribution function of the exchange interactions $P(\mathcal{J})$ and the corresponding $M(H)$ magnetization curve: **(a)** disordered ferromagnetism, **(b)** asperomagnetism, **(c)** speromagnetism and **(d)** spin glass.

Fig. A1. XRD pattern of the hexagonal Tb-Dy-Ho-Er-Tm HEA at RT, using Cu $K\alpha_1$ radiation ($\lambda = 1.54056$ Å). The peaks are indexed to a hcp crystal lattice.

Fig. A2. A SEM backscattered-electron image of the TDHET polygrain sample, showing the microstructure of differently oriented crystalline grains due to the channeling contrast.

Fig. B1. Electrical resistivity $\rho(T)$ of the TDHET between RT and 2 K in magnetic fields $0 - 9$ T. The inset shows the magnetic-field dependence of the resistivity on an expanded scale between 150 and 90 K.

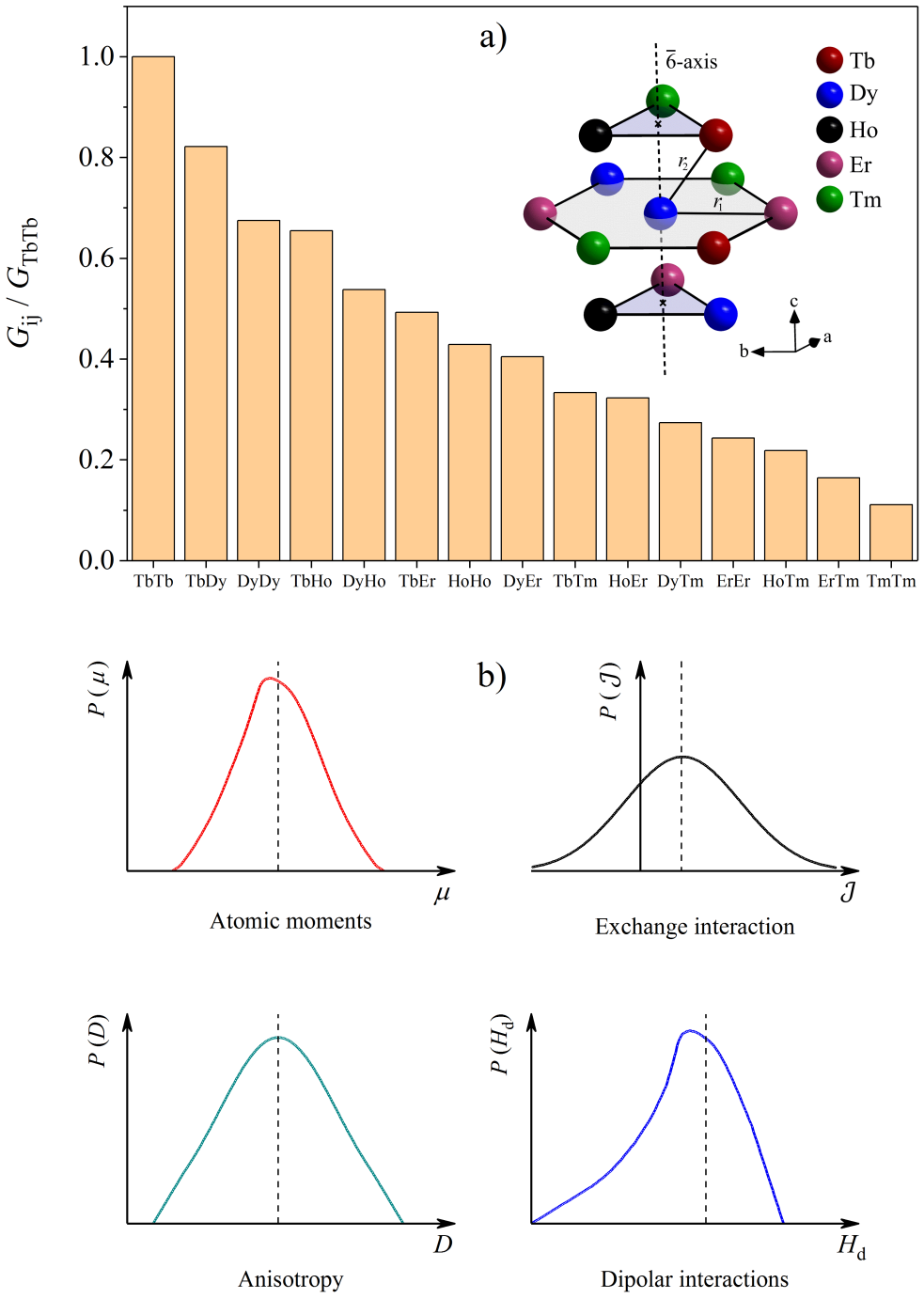
a)
G_{ij} / G_{TbTb}
1.0
0.8
0.6
0.4
0.2
0.0
TbTb TbDy DyDy TbHo DyHo TbEr HoHo DyEr TbTm HoEr DyTm ErEr HoTm ErTm TmTm
$\bar{6}$-axis
r_2
r_1
Tb
Dy
Ho
Er
Tm
c
a
b
b)
$P(\mu)$
μ
Atomic moments
$P(\mathcal{J})$
$\mathcal{J}$
Exchange interaction
$P(D)$
D
Anisotropy
$P(H_d)$
H_d
Dipolar interactions

Fig. 1

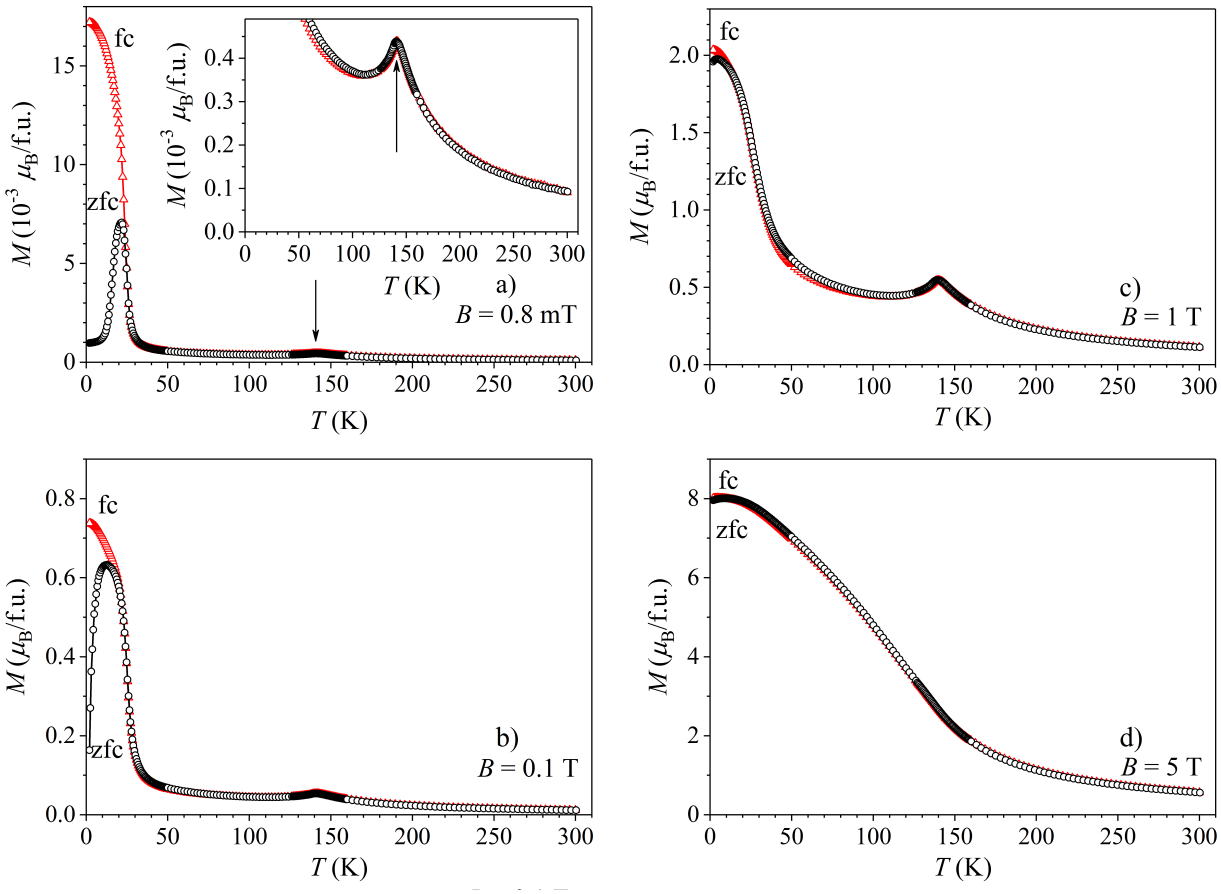

Fig. 2

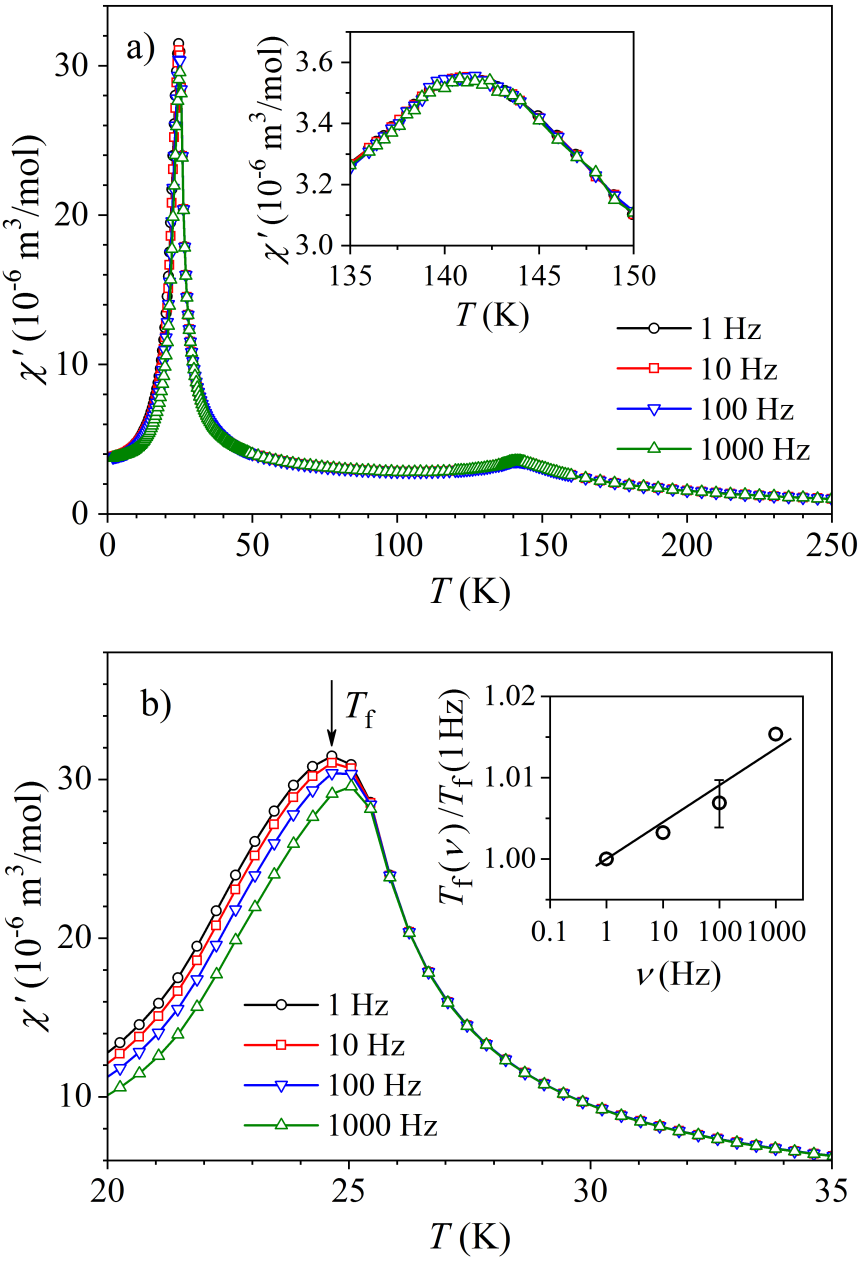

Fig. 3

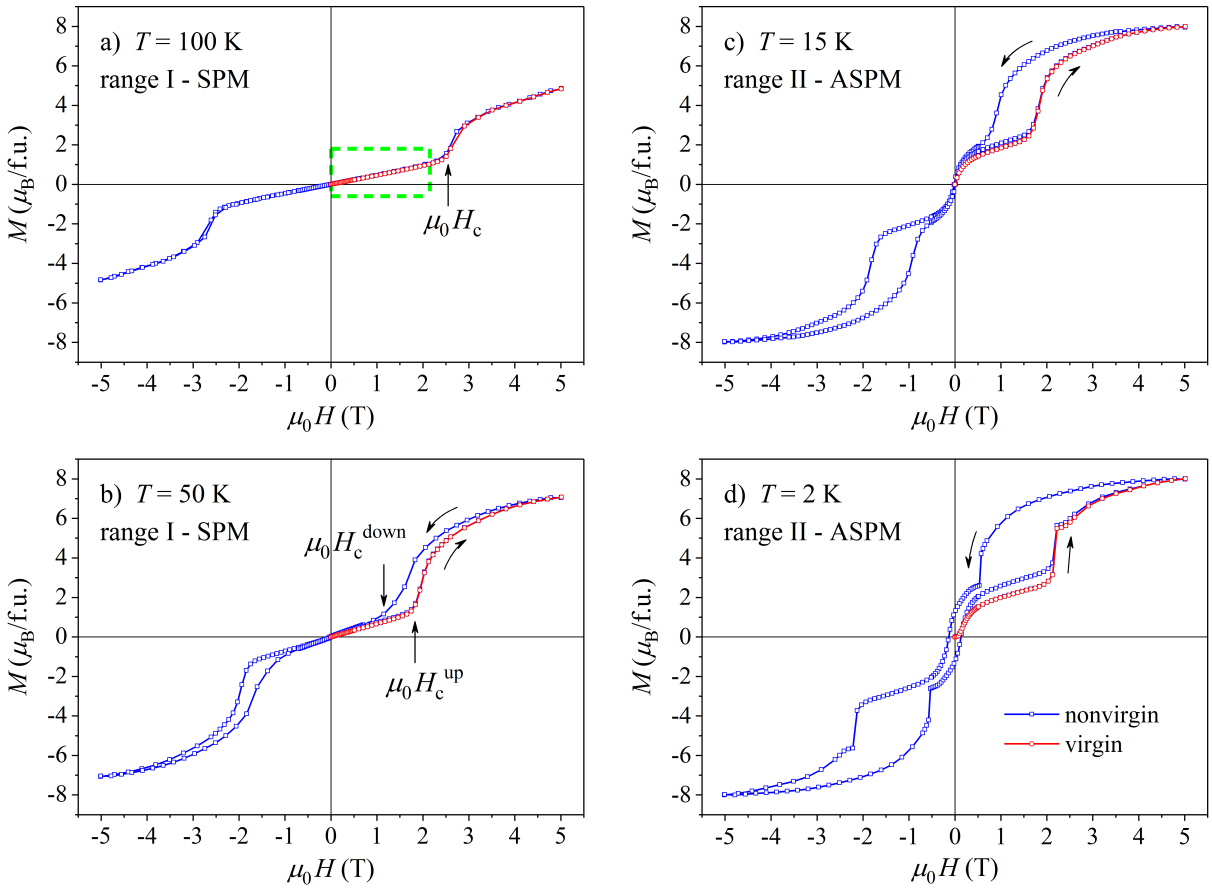
a) T = 100 K
range I - SPM
μ0Hc
M (μB/f.u.)
μ0H (T)
b) T = 50 K
range I - SPM
μ0Hc down
μ0Hc up
c) T = 15 K
range II - ASPM
d) T = 2 K
range II - ASPM
nonvirgin
virgin

Fig. 4

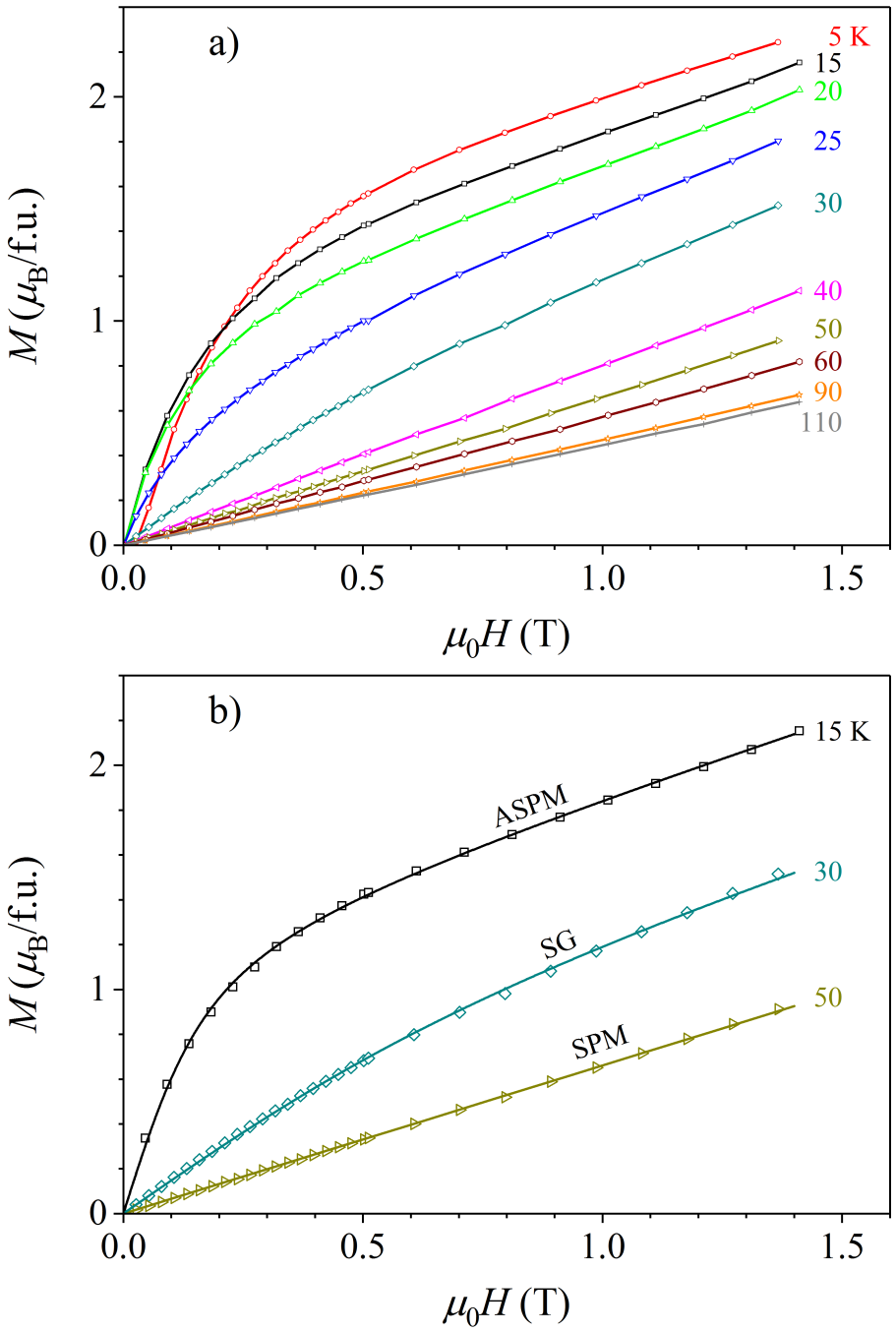
a)
5 K
15
20
25
30
40
50
60
90
110
$M\,(\mu_B/\mathrm{f.u.})$
$\mu_0 H$ (T)
b)
15 K
30
50
ASPM
SG
SPM
$M\,(\mu_B/\mathrm{f.u.})$
$\mu_0 H$ (T)

Fig. 5

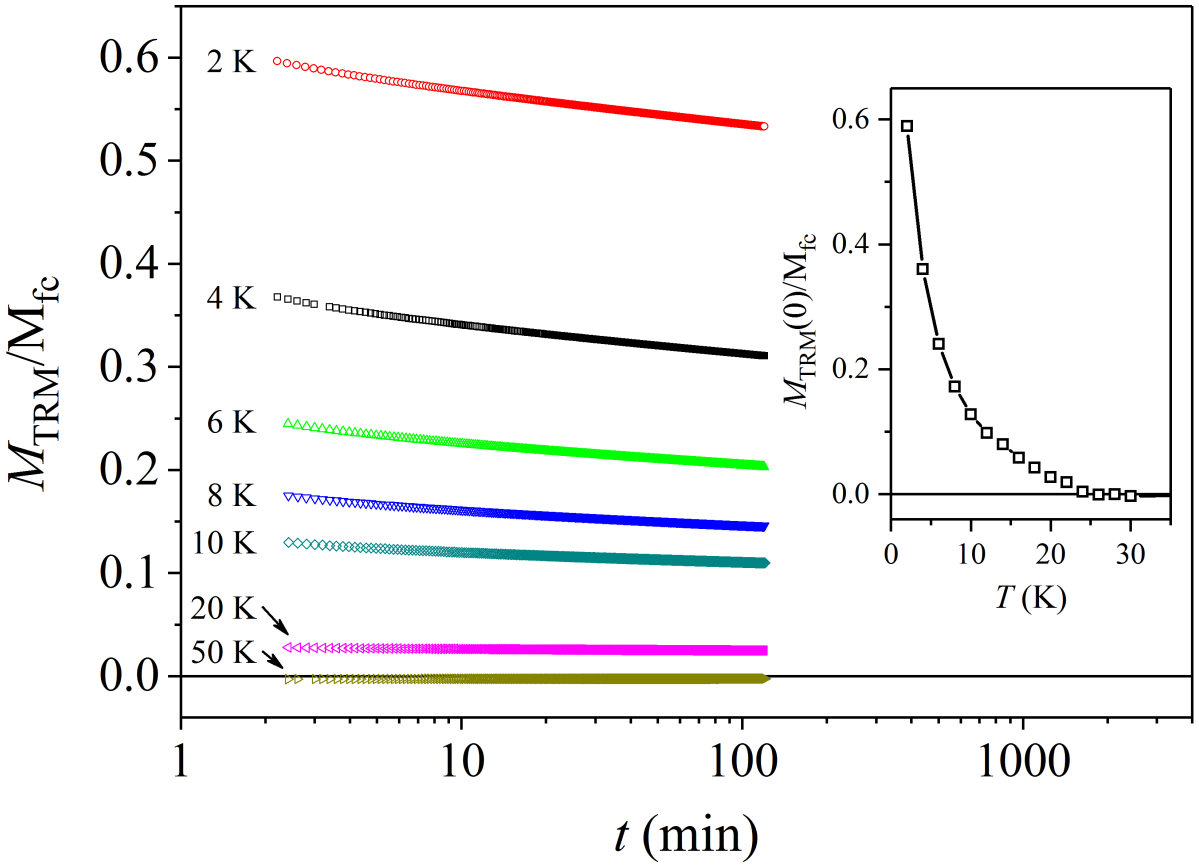
0.6
0.5
0.4
0.3
0.2
0.1
0.0
2 K
4 K
6 K
8 K
10 K
20 K
50 K
1
10
100
1000
t (min)
M_TRM/M_fc
M_TRM(0)/M_fc
0.6
0.4
0.2
0.0
0
10
20
30
T (K)

Fig. 6

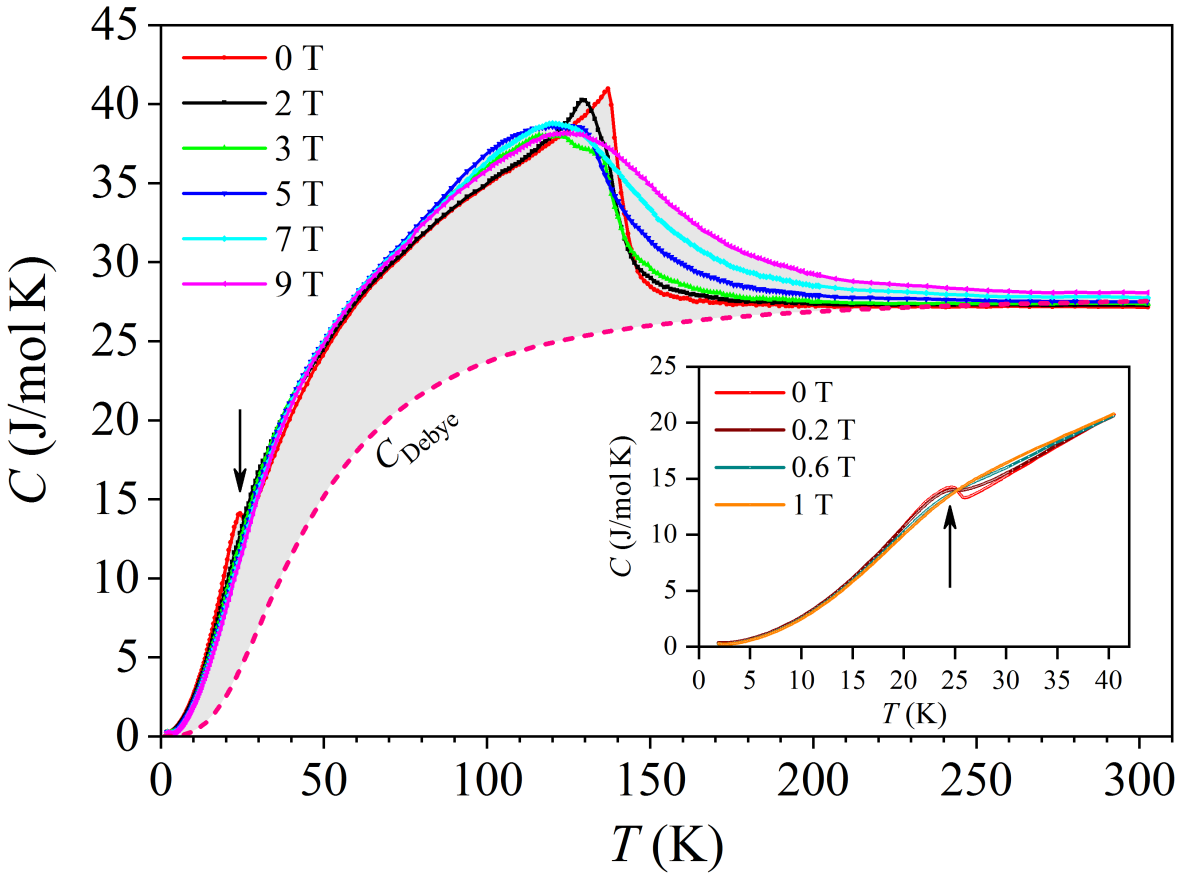

Fig. 7

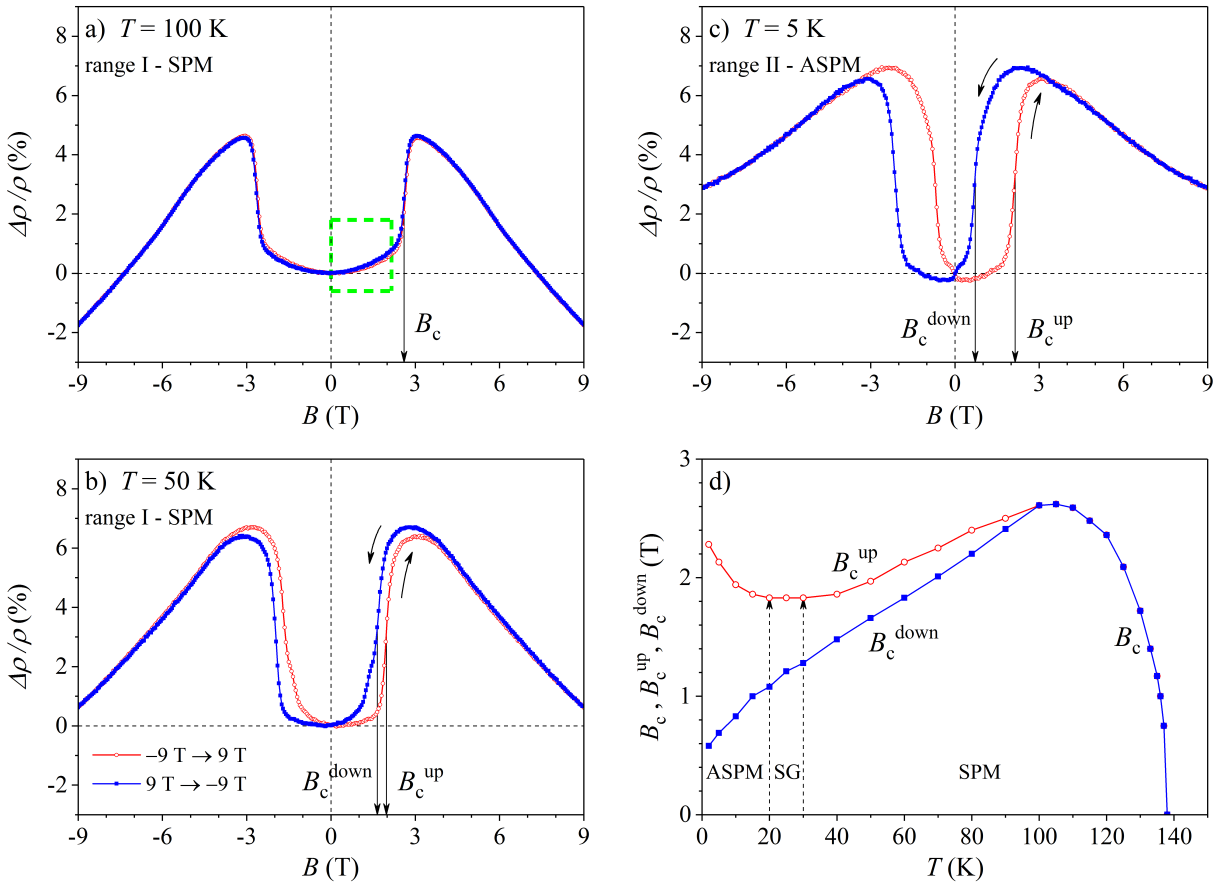
a) T = 100 K
range I - SPM
Δρ/ρ (%)
B (T)
B_c
b) T = 50 K
range I - SPM
–9 T → 9 T
9 T → –9 T
B_c^down
B_c^up
c) T = 5 K
range II - ASPM
d)
B_c , B_c^up , B_c^down (T)
T (K)
ASPM
SG
SPM

Fig. 8

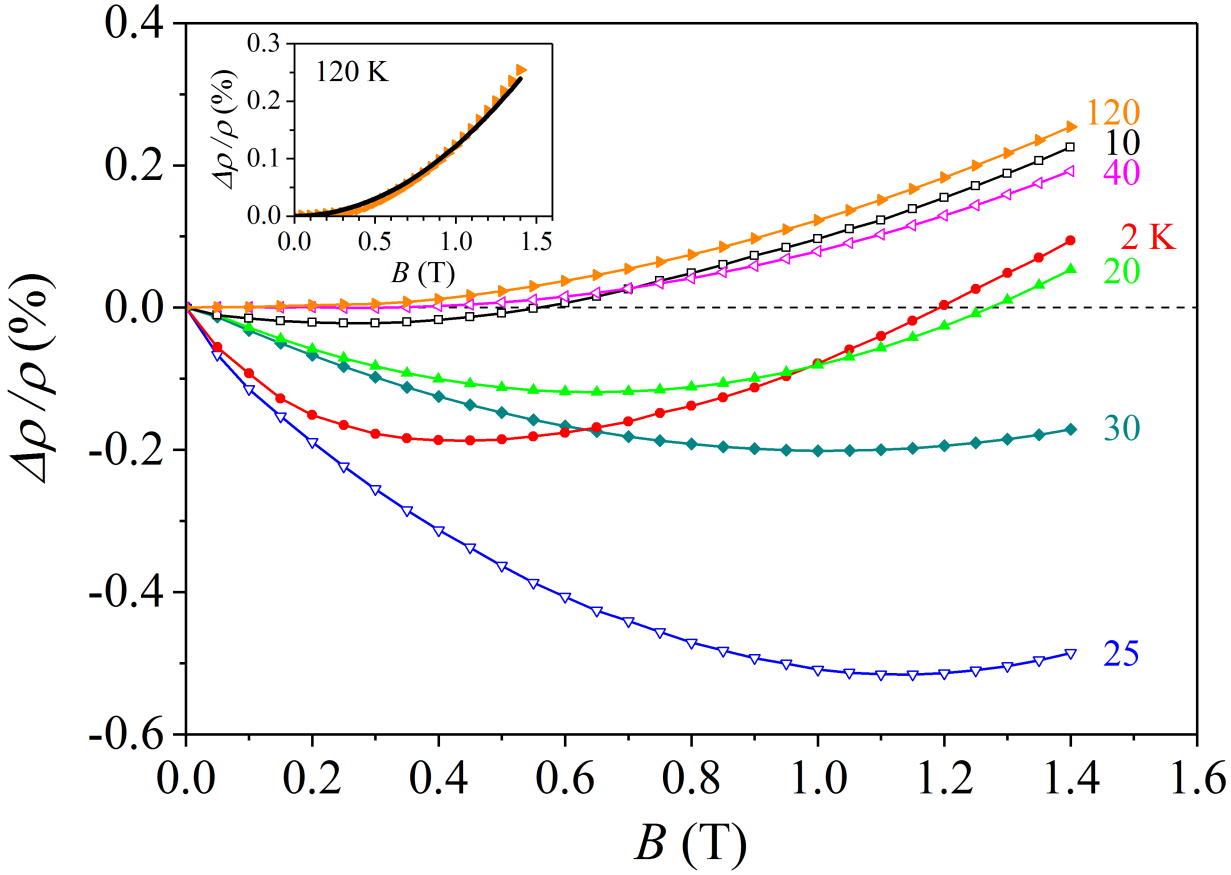
0.4
0.2
0.0
-0.2
-0.4
-0.6
0.0
0.2
0.4
0.6
0.8
1.0
1.2
1.4
1.6
Δρ/ρ (%)
B (T)
120
10
40
2 K
20
30
25
120 K
0.3
0.2
0.1
0.0
0.0
0.5
1.0
1.5
Δρ/ρ (%)
B (T)

Fig. 9

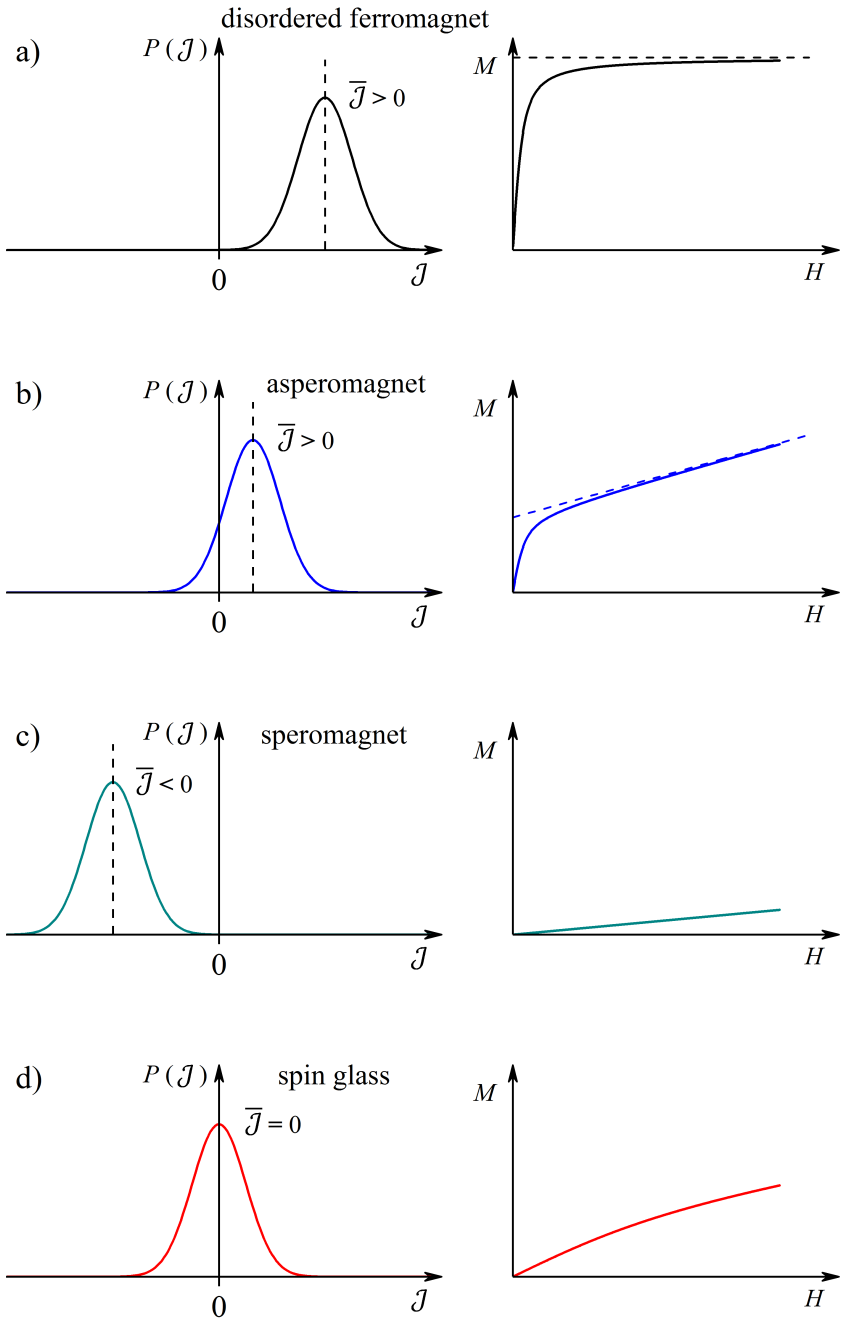
a)
disordered ferromagnet
P(J)
$\overline{J} > 0$
0
J
M
H
b)
asperomagnet
P(J)
$\overline{J} > 0$
0
J
M
H
c)
speromagnet
P(J)
$\overline{J} < 0$
0
J
M
H
d)
spin glass
P(J)
$\overline{J} = 0$
0
J
M
H

Fig. 10

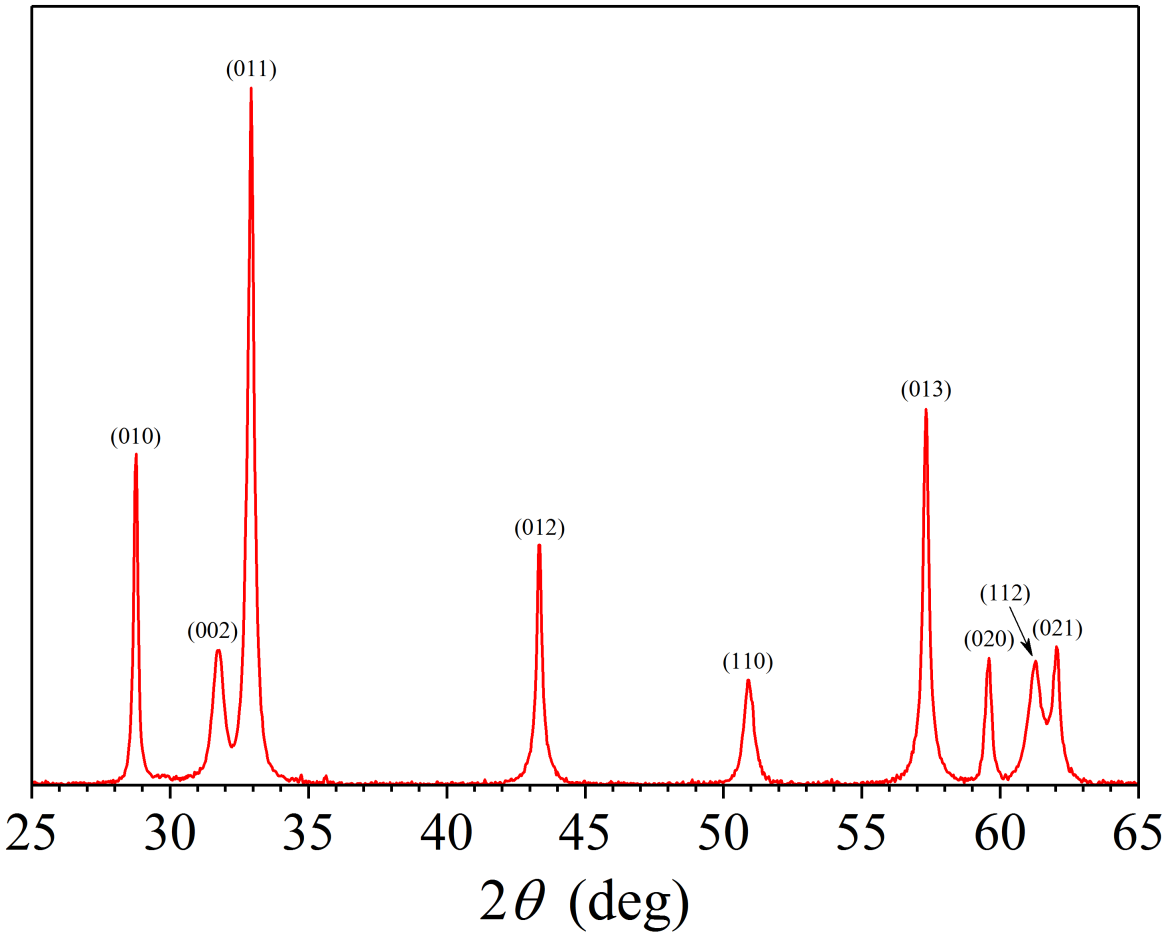
(011)
(010)
(002)
(012)
(110)
(013)
(112)
(020)
(021)
25
30
35
40
45
50
55
60
65
2θ (deg)

Fig. A1

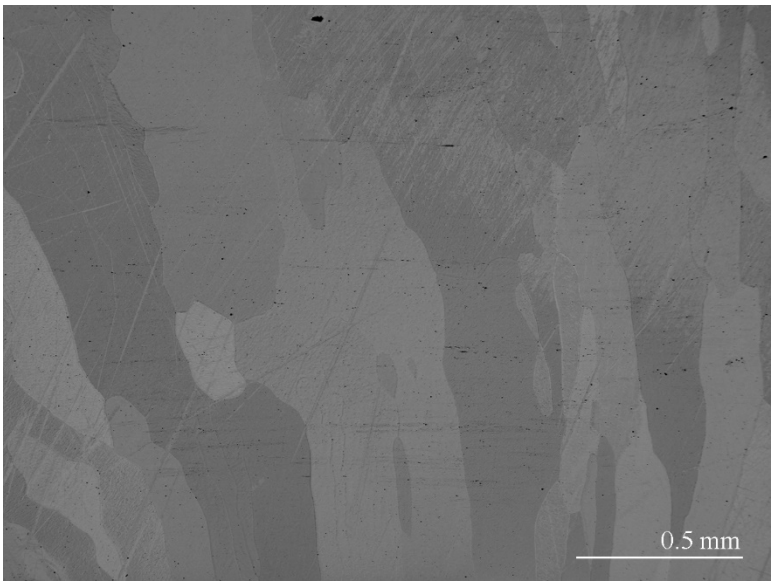

Fig. A2

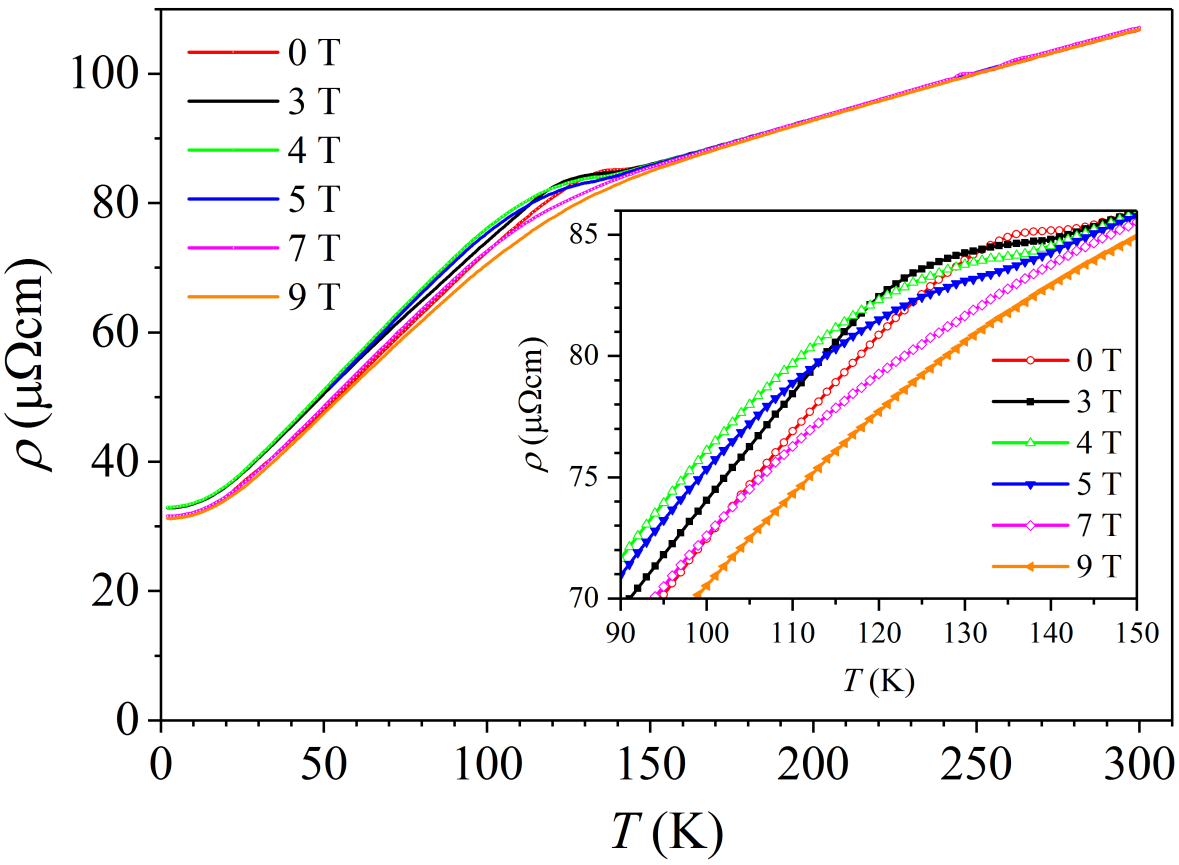
0 T
3 T
4 T
5 T
7 T
9 T
ρ (μΩcm)
T (K)
0
20
40
60
80
100
0
50
100
150
200
250
300
85
80
75
70
90
100
110
120
130
140
150

Fig. B1